Physico-chemical parameter measurement and model response evaluation for a pseudo-two-dimensional model of a commercial lithium-ion battery

L. Oca [a],[*], E. Miguel [a], E. Agirrezabala [a], A. Herran [b], E. Gucciardi [b], L. Otaegui [b], E. Bekaert [b], A. Villaverde [b], U. Iraola [a]

[a] Mondragon Unibertsitatea, Electronic and computing department, 4 Loramendi, Basque Country, Mondragon 20500, Spain
[b] Centre for Cooperative Research on Alternative Energies (CIC energiGUNE), Basque Research and Technology Alliance (BRTA), Alava Technology Park, Albert Einstein 48, Vitoria-Gasteiz 01510, Spain

ARTICLE INFO

ABSTRACT

To effectively evaluate battery performance by means of electrochemical modelling, a consistent set of parameters is essential. The aim of this work is to provide a complete physico-chemical methodology to measure all the necessary parameters for a pseudo-two-dimensional (P2D) electrochemical model. Component composition, thermodynamic, kinetic and transport properties, parameters related to the porous structures, internal battery configuration and full-cell electrode balancing are presented for a commercial lithium-ion battery. Then, the measured parameters are entered into the P2D model, and battery responses are evaluated against full-cell experimental curves (galvanostatic charge-discharge at different current rates, EIS responses and pulses) to correlate numerical-experimental results.

© 2021

1. Introduction

In recent years, a great effort is being dedicated to apply computational techniques to improve electrochemical energy storage systems [1]. In fact, devices such as lithium-ion batteries are exponentially growing in the market [2]. The development of new cells and individual component design, fabrication processes and materials in the energy storage field has mainly been achieved based on experimental work for years [3]. As this approach consumes a large amount of resources (time and money) a suitable design of experiments should be defined which efficiently studies the most relevant process parameters. Nevertheless, the number of experiments are limited, experimental approach should be enhanced looking at a long-term solution [3]. Modelling as an advanced technique to improve the design and fabrication process of electrochemical energy storage systems is then a key research field. It is important to combine experimental and numerical analysis as a way to validate models capable of assisting battery design and development.

The electrochemical model can help understanding the mechanisms occurring inside a battery and is generally based on the mathematical framework developed by Newman et al. [4–9]. It is based on the porous electrode theory and concentrated solution theory. More detailed information of the P2D model description can be found in literature [4–10]. This model can simulate any dual insertion cell if physical properties and system parameters are provided. However, a coherent set of parameters is necessary to obtain accurate and reliable predictions [7].

Two different approaches can be followed in order to determine model parameters: computational identification and physico-chemical parameter measurement methods [11]. In the computational approach, model parameters are identified based on one data set (single-objective optimisation routine [12–14]) or multiple data sets (multi-objective optimisation routines [10,14–16]) that are experimentally measured (normally voltage, current and temperature responses). In most of the cases, the required experimental data is collected from a commercial cell using non-invasive techniques, although some authors proceed to open it and measure directly parameters such as geometrical [15] and Open Circuit Voltage (OCV) curves [10,15,16]. These methods provide a set of parameters with less infrastructure but higher computational cost. However, these methods could find difficulties to determine all the inherent properties of the materials due to the complex interactions between parameters [10,14–16]. In the physico-chemical approach,

* Corresponding author at: Mondragon Unibertsitatea, Electronic and computing department, 4 Loramendi, Basque Country, Mondragon 20500, Spain.
E-mail address: lauraoca@mondragon.edu (L. Oca).

the cell is opened and physico-chemical tests are performed to determine the parameters corresponding to all the battery components.

In the literature, two subgroups can be distinguished within the physico-chemical approach: partial and full parameter measurement methodologies. On the one hand, partial characterizations are commonly found in the literature [7,17–21]. Generalizing, these methods consist of cell opening and performing a basic physico-chemical characterization (geometrical parameter measurement, electrode OCV measurement, full-cell electrode balancing estimation and microstructural/composition analysis by SEM/EDS). However, transport and kinetic parameters are usually estimated or taken from other sources. Thus model variable predictions, especially dynamic responses are not accurate, although the voltage response behaves similar to the experimentally measured data for galvanostatic charge-discharge processes. On the other hand, only few articles show an almost complete physico-chemical characterization and explain the procedure followed to obtain the parameters [6,7,23–28]. This work is focused in the definition of a full parameter measurement methodology for a P2D model.

Doyle et al. [6,7] explained the parameter measurement procedure and the physico-chemical techniques that could be applied for a dual-insertion cell. Authors stated that further work needs to be accomplished in this field so as to study the suitability of different characterization techniques and increase the equipment accuracy. The parameter measurement complexity could increase if temperature, state of charge, local concentration etc. are taken into account. Moreover, Ecker et al. [23–25] obtained model parameters and implemented the model as a proof of the correctness of the set of parameters. Finally, Schmalstieg et al. [26–28] enhanced Ecker et al. parameterization [23–25] proposing a different methodology for full-cell electrode balancing determination and including information about the electrolyte.

Due to low amount of works related to this field, there is a considerable research gap in order to standardize the physico-chemical parameter measurement methodology. The aim of this work is to provide a replicable and complete methodology to obtain all the necessary parameters needed as an input for an electrochemical model. Moreover, a complete validation procedure with invasive and non-invasive tests is provided. This paper also gives an insight of the sample preparation, measurement techniques and result extraction for each model parameter. Finally, the next steps towards this type of characterisation considering cell-to-cell variability is assessed based on the results of this methodology. Furthermore, this work provides all the parameter values needed for an electrochemical model of a commercial lithium-ion battery.

In this research paper, first, the full physico-chemical parameter measurement methodology is introduced. Then, the results obtained based on the proposed methodology are presented: component composition, thermodynamic and kinetic parameters, transport properties, parameters related to the porous structures, cell internal configuration and full-cell electrode balancing determination. Finally, model response evaluation (galvanostatic charge-discharge at different current rates, EIS responses and pulses) is discussed comparing simulated and experimental full-cell results.

2. Physico-chemical parameter measurement methodology and sample preparation

Fig. 1 shows an overview of the procedure implemented to obtain all the model parameters. There, a summary of the measured parameters together with the type of sample under study and the characterization techniques are presented. All the parameters used in Fig. 1 that are needed to fully define the P2D model are described in the list of symbols. Moreover, the techniques used for the physico-chemical characterization are presented in the Appendix A, in which the associated character (used in Fig. 1), the acronym, the full name of each technique and the equipment used in this work is gathered.

It is worth noting that, for some parameters, more than one technique was used for verification or adding information. The parameters were divided into five groups, as highlighted in grey in Fig. 1. First, the component composition was determined (I). Second, thermodynamic and kinetic parameters were extracted (II). Third, the transport properties were obtained (III). Then, parameters related to the porous structures and adjustable design parameters were characterized (IV). Finally, full-cell electrode balancing, and internal configuration of the battery is described (V).

Two commercial cells were taken for the physico-chemical characterization. The first cell was fully discharged at C/10 until the lower cut-off voltage (2.7 V). The other cell was fully charged at C/10 until the upper cut-off voltage (4.2 V). The disassembly of the cells was done within 3 h of the cycling procedure. The same methodology explained by Waldmann et al. [29] was used for dismantling the cells. The cells were opened inside an Ar filled glove box (O_2 < 0.1 ppm and H_2O < 0.1 ppm, Jacomex) as the samples are reactive to O_2 and H_2O.

The electrolyte extraction was performed during cell opening. Due to the high cost of electrolyte (9.9 to 16 % of the battery cost) among other reasons, manufacturers tend to optimise, reducing the amount of electrolyte to the minimum [27]. In commercial pouch cells there is usually no excess of electrolyte. Therefore, in this work, after the cell was opened, a sample including both electrodes and separator (all impregnated in electrolyte) were rapidly immersed in dichloromethane and then analysed with Gas Chromatography-Mass Spectrometry (GC-MS) technique. A similar procedure was used by Pilipili [30].

After the electrolyte extraction, all the battery components were separated. Unit samples of the separator, positive and negative electrodes to be studied were carefully selected to collect a representative sample with no visual defects, and washed with dimethyl carbonate to perform the remaining physico-chemical tests. The electrodes were then analysed so as to define the parameters related to the porous structures (i.e. porosity, specific surface area and tortuosity). Additional sample preparation was required for techniques such as XRD, ICP-IOS, TGA, PSA, and electronic conductivity in which electrodes were scratched and the recovered powder was analysed. Finally, the punched electrodes were reassembled into reconstructed coin cells in an argon filled glove box to perform the electrochemical measurements. First of all, one side coating of the electrodes was removed with N-Methyl-2-pyrrolidone. Then, different types of cells were constructed (half coin cells, full coin cells and polarization cells). The configuration and materials of the studied cells are listed below:

- **Full coin cells (CR2032):** 12 mm diameter one side coated positive and negative electrodes separated by a Whatman glass fibre (Grade GF/D) separator of 16 mm impregnated with 1 M $LiPF_6$ in EC:EMC (50:50 v%) LP50 (battery grade, Sigma Aldrich) electrolyte (EC: ethylene carbonate; EMC: ethyl methyl carbonate).
- **Half coin cells (CR2032):** a 12 mm diameter one side coated positive or negative electrode and a 12 mm diameter lithium metal disc separated by a Whatman glass fibre (Grade GF/D) separator of 16 mm impregnated with 1 M $LiPF_6$ in EC:EMC (50:50 v%) LP50 (battery grade, Sigma Aldrich) electrolyte.
- **Polarization cell (CR2032):** symmetrical lithium metal discs of 12 mm of diameter separated by a 16 mm diameter separator of the cell under study impregnated with 1 M $LiPF_6$ in EC:EMC (50:50 v%) LP50 (battery grade, Sigma Aldrich) electrolyte.

The polarization cell was constructed in order to study the electrolyte and separator properties (i.e. effective conductivity in the separator, Bruggeman coefficient, tortuosity and porosity), taking as a reference specific works dealing with polymer and separator characterization [31]. In the remaining cells, the separator was not from the cell under study. In full and half coin cells, and T-cells Whatman glass fibre
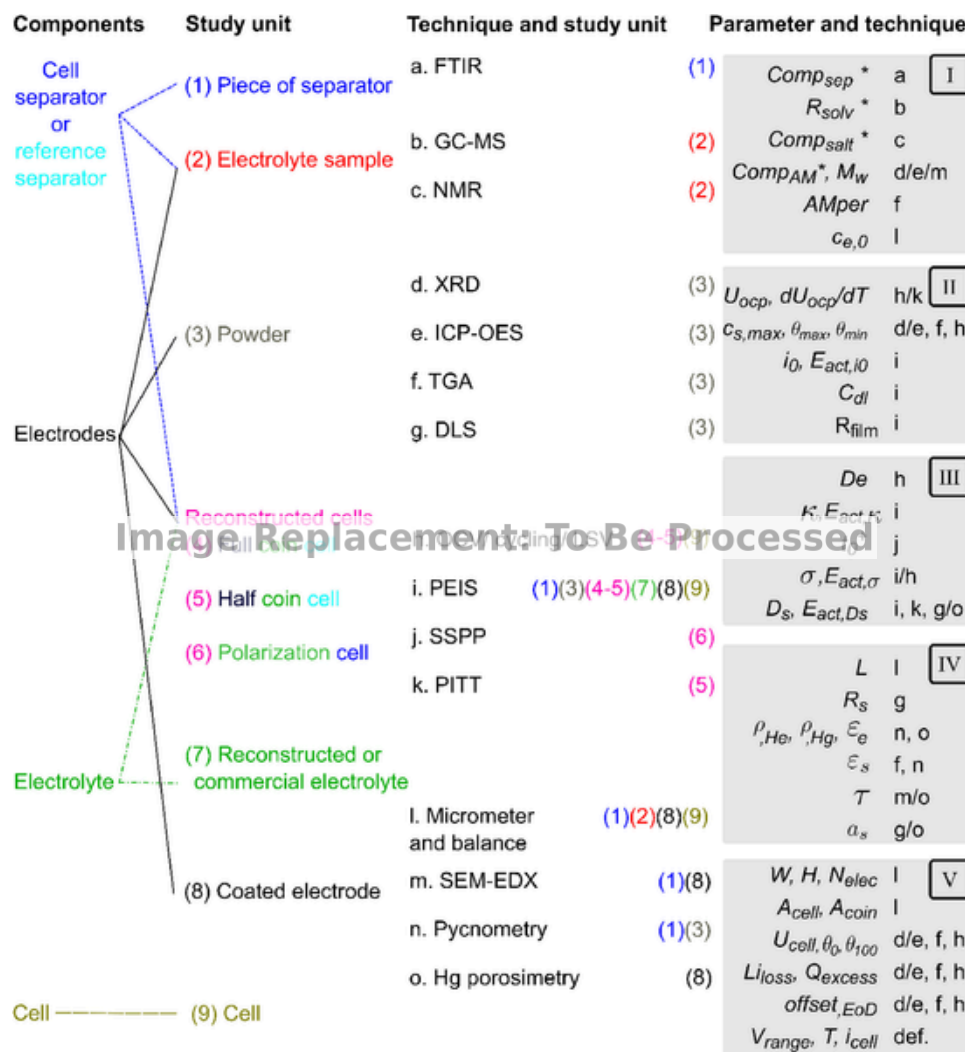
Fig. 1. Schematic representation of the full physico-chemical parameter measurement methodology. Parameter groups are presented in grey boxes: I. Component composition (*not used directly as a parameter for the model, but necessary for verification of the datasheet), II. Thermodynamic and kinetic parameters, III. Transport properties, IV. Parameters related to the porous structures and adjustable design parameters and V. Cell internal configuration and electrode balancing determination.

(Grade GF/D) separators were used because these are commonly used in the literature thereby reducing the uncertainty of the analysed system [22–27,30].

3. Theoretical framework

In order to evaluate the validity of the proposed experimental methodology, the measured parameters were implemented into a pseudo-two dimensional (P2D) model in COMSOL Multiphysics® simulation software (version 5.5). This model is based on the mathematical framework developed by Newman et al [6,7]. Detailed information about the geometry, governing equations, boundary conditions and parameters can be found in [4–10] for time-domain and [38,39] for frequency-domain.

4. Results and discussion

The proposed methodology was applied to a 1.25 Ah high power commercial cell so as to test its efficacy. This section is divided into six parts: (1) component composition; (2) thermodynamic and kinetic parameters; (3) transport properties, (4) parameters related to the porous structures and adjustable design parameters, (5) cell internal configuration and electrode balancing determination, and (6) model response evaluation.

4.1. Component composition

Firstly, the component identification was performed for all the materials (electrodes, separator and electrolyte) using the techniques presented in Fig. 1.

In order to determine the active material (AM) composition of both electrodes, the XRD technique was used, which was complemented with ICP-IOS and SEM-EDS in the positive electrode. The analysis was performed with the cell opened at the discharged state (0 % SoC), which corresponds to an almost delithiated negative electrode and almost lithiated positive electrode. The negative powder XRD pattern analysis shows that the electrode is composed of graphite (for the discharged cell) (see Fig. S1 (a)). The positive powder XRD pattern (see Figure S1 b)) clearly shows that the sample contains two phases. The refined parameters for the Phase 1 ($a = b = 2.851(6)$ Å, $c = 14.214(2)$ Å, $\alpha = \beta = 90°$, $\gamma = 120°$) can be compared with cell parameters of $Li_yNi_{0.8}Co_{0.15}Al_{0.05}O_2$ (NCA) [35], whereas the refined parameters for Phase 2 ($a = b = 2.816(7)$ Å, $c = 14.017(2)$ Å, $\alpha = \beta = 90°$, $\gamma = 120°$) can be related to Li_yCoO_2 (LCO) [36]. A small amount of graphite [37], which could be used as a conductive additive, was also identified in the

positive electrode diffraction pattern (see Fig. S1 b)). The fact that the c parameter of Phase 1 is larger than those reported in the literature suggests that Phase 1 is partially delithitated. Indeed the delithiation of the layered $LiMO_2$ phases (M = Ni, Co, Mn or combination of them) is known to produce an increase in the c cell parameter (due to an increase of electrostatic repulsion between the anions [38]).

The obtained results are in good concordance with Mayur et al. [39] who analysed the positive electrode composition by means of the SEM-EDS technique for a similar battery (kokam 0.35 Ah, reference SLPB283452H) and reported a compound based on a blend between NCA and LCO particles. Moreover, Fuchs et al. [40] studied the composition of a 3.3 Ah kokam battery (reference SLPB526495) with the ICP-OES and SEM-EDS techniques, obtaining an average composition of $LiNi_{0.64}Co_{0.35}Al_{0.01}O_2$ (ICP-OES results). The elements reported by these authors are in good agreement with the ICP-OES results of the analysed cell of this paper, although the identified ratios differ (0.40 ± 0.05 of nickel, 0.56 ± 0.04 of cobalt and 0.03 ± 0.03 of aluminium). The identified aluminium content was slightly higher than the expected values due to the preparation of the experimental test (scratching process). As stated in Fuchs et al. [40], the aluminium content could also be due to current collector contamination during the ICP-OES sample preparation. Nevertheless, SEM-EDS mapping was performed in which the two-phase blend was clearly visible, and it was thus possible to confirm the aluminium content of Phase 1 (see Fig. 2 a)). A ratio between the two phases can be estimated with the ICP-OES results. Therefore, a composition of 50 ± 2 % of $LiCoO_2$ and 50 ± 2 % of $LiNi_{0.8}Co_{0.15}Al_{0.05}O_2$ was identified for the blended active material.

In addition, thermogravimetric analysis was conducted in order to determine the AM percentage of the electrode coatings, which directly affects into the cell theoretical capacity calculation. The active material

percentage calculations are based on the mass loss during the heating process corresponding to:

- Water evaporation (until 373.15 K)
- Binder decomposition (minimum mass to time derivative in a range between 673.15 K and 773.15 K for binders composed of PVDF, with a minimum peak around 723.15 K [41]; pyrolysis of the SBR elastomer between 573.15 and 823.15 K, with a minimum peak around 753.15 K [42]; and CMC with a minimum peak around 573.15 K [43])
- Conductive additive decomposition (up to 9 % and 24 % of mass loss at 815 K of a similar graphite and carbon black (C65), respectively).

In the negative electrode (see Fig. S2 a)), we identified mass to time derivative minimums at 584.15 K and 753.15 K which could correspond to CMC and SBR binders, respectively. A small quantity of carbon black can be expected (around 1 %), which was degraded before 584.15 K. Therefore, the negative electrode is composed of 95 ± 3 % graphite, 3 ± 2 % of CMC/carbon black and 2 ± 2 % of SBR. In the positive electrode (see Fig. S2 b)), we identified mass to time derivative minimums at 700.15 K and 815.15 K which could be related to a binder composed of PVDF and graphite additive, respectively (a small quantity of graphite was expected based on the results obtained from the XRD pattern refinement). The formulation of the positive electrode was found to be 93 ± 2 % of LCO/NCA, 3 ± 2 % of PVDF and 4 ± 2 % of graphite additive/carbon black (from that 4 % a small amount of carbon black was expected (around 1– 2%)). For both electrodes, similar formulations are found in the literature [44]. Even if it is possible to correlate the mass to time derivative as a function of the temperature for the expected materials in each electrode, it is worth mention-
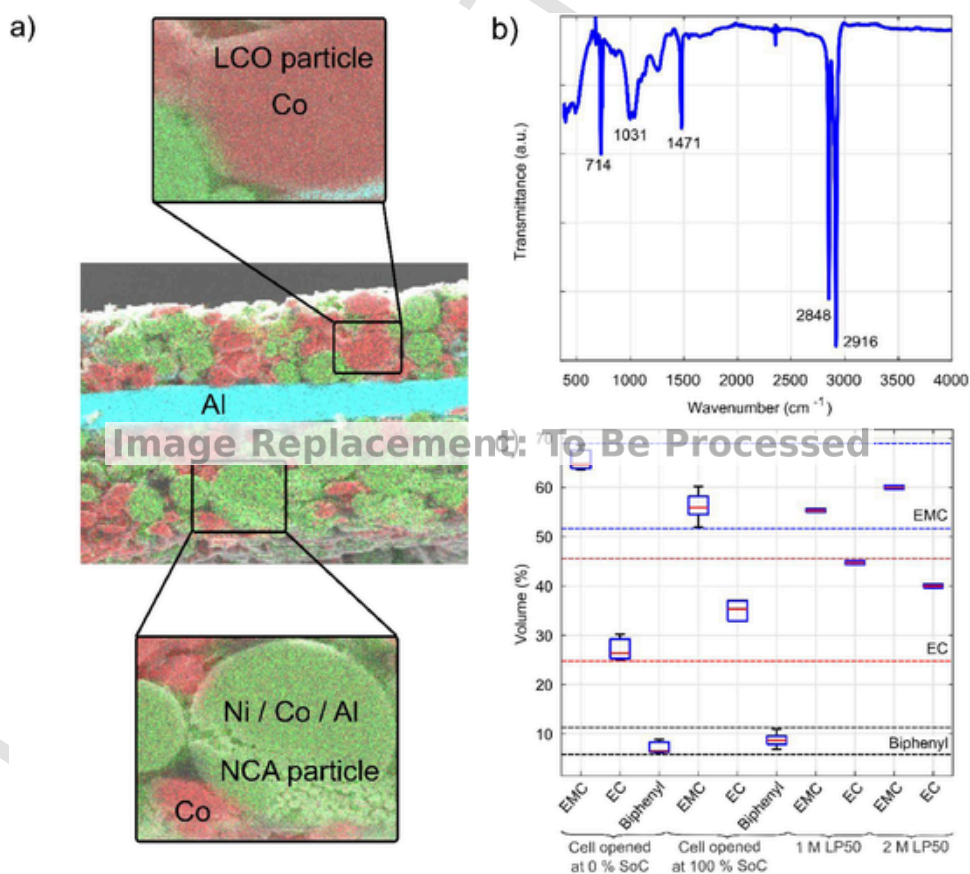

Fig. 2. (a) EDS mapping of the blended positive electrode, showing Ni, Co and Al in a general cross-sectional view of the electrode and zoomed into LCO and NCA particles; (b) FTIR analysis of the separator and (c) GC-MS analysis of the sampled electrolyte.

ing that the decomposition processes are a characteristic of the tested specific materials. As no previous information of the materials is available, the uncertainty of this technique is high.

In order to characterize the separator film, FTIR (see Fig. 2 b)) was performed. The FTIR spectrum was compared with literature which indicates that the characteristic absorbance bands of polyethylene (PE) are located at 2914 cm^{-1}, 2847 cm^{-1}, 1470 cm^{-1} and 718 cm^{-1} [45]. The characteristic bands of the analysed sample were obtained at 2916 cm^{-1}, 2848 cm^{-1}, 1471 cm^{-1} and 714 cm^{-1}. A non-identified peak is located at 1031 cm^{-1}, which could be due to electrolyte traces. The FTIR result confirms that the separator composition is PE, which differs from the datasheet. The manufacturer reports that the separator is composed of PVDF, which is a thin coating layer that could be added as a safety agent to prevent short-circuits [46].

For the electrolyte characterization, GC-MS and NMR techniques were used, for electrolyte solvent ratio and salt composition identification, respectively. Both opened cells, at charged and discharged states were analysed by GC-MS. In this technique, it should be taken into account that the list of the identified components and ratios are not precise, as the evaporation process of the solvents under Argon atmosphere is not negligible [32]. The volume percentages of the detected elements are shown in Fig. 2 c), in which the dispersion between measurements is also plotted. The solvents that were identified are Ethyl Methyl Carbonate (EMC) and Ethylene Carbonate (EC) which are in good agreement with the datasheet. We also found biphenyl traces in the analysed samples. Biphenyl is commonly used as a fire-retardant additive in LIBs [32]. The dotted lines correspond to the maximum and minimum values obtained for each of the components. A range between 50 - 70% for EMC (blue), 25 – 45 % for EC (red) and 5 -10% Biphenyl (black) were found. Additionally, a 1 M and 2 M LiPF$_6$ EC/EMC (50/50 %v) commercial electrolytes (LP50) were characterized for comparison purposes.

^{19}F and ^{31}P NMR spectra were recorded to confirm that the electrolyte salt is LiPF$_6$, as expected from the datasheet. Comparing our results with those obtained from the commercial electrolytes, it is possible to approximate the sample electrolyte to LiPF$_6$ EC/EMC (50/50 %v) or LiPF$_6$ EC/EMC (30/70 %v) with a small percentage of biphenyl additive. The electrolyte identification allowed us to use a similar electrolyte in the remaining characterization procedures.

An accurate determination of the salt concentration is not possible if a sample of the bare electrolyte (not impregnated in the separator) cannot be extracted from the cell. If there is an excess of electrolyte, a known volume can be analysed by NMR for a quantitative analysis (which requires internal references), although interpretation of the results should be carefully analysed due to the decomposition products of the LiPF$_6$ (i.e., LiF) [47] or the solvents [48]. Unfortunately, no electrolyte could be recovered from this specific cell; therefore, electrolyte salt concentration was calculated by means of weight differences between cleaned and not cleaned electrodes, applying the Eq. (1).

$$c_{e,0} = \frac{m_{no-clean} - m_{clean}}{V_{external} - V_{inactive} + V_{extra}},$$

(1)

where the $V_{external}$ is the total external volume of the cell (43 × 75 × 5.3 mm), $V_{inactive}$ represents the inactive parts of the components (current collector, separator and electrode solid-phase volumes (ε_s)) and V_{extra} represents the added extra volume in the pouch cell filling step process.

A value of 2 ± 0.5 M was calculated without including any extra electrolyte volume. However, in the electrolyte filling process, extra electrolyte is added into the process (if 3 mL extra are added, a value of 1.5 ± 0.5 M was obtained) and during the formation cycles some lithium ions get trapped into the electrodes irreversibly and decomposition products are produced and removed during the degassing process. This leads to the conclusion that the uncertainty of this procedure is high as the calculation are based on indirect measurements and results are based on the weighted salt of the cell after the formation cycles of the cell.

4.2. Thermodynamic and kinetic parameters

The thermodynamic and kinetic parameters accounts for the OCV curve, the film resistance, the charge transfer resistance, and the double layer capacitance for each half reaction as a function of the state of lithiation (SoL) and temperature.

Quasi-steady-state curves (qOCV) were obtained by means of galvanostatic charge-discharge processes at C/30. Additionally, potentiostatic intermittent titration technique (PITT) was used to show the suitability of qOCV curves [49]. It is well known that OCVs present a dependency on the temperature and hysteresis [49]. Therefore, both tests were performed at three temperatures (278.15, 298.15 and 318.15 K). Moreover, in order to reduce the introduced error into the model due to hysteresis effect, charge and discharge curves were averaged following the procedure proposed by Schmalstieg et al. [27]. First, the charge and discharge curves were split at half experimental capacity into two pieces each (low and high lithiation ranges, which corresponds to high and low voltage ranges, respectively). In that point (half experimental capacity), the difference between charge and discharge curves was calculated. Then, low lithiation range of the charge process and high lithiation range of the discharge process were shifted by half the voltage difference to obtain the averaged OCV curve. The results for negative and positive electrodes are shown in Fig. 3 (a) and (b), in which experimental points from PITT and charge-discharge averaged OCV curves are presented. The temperature dependency is taken into account with the voltage to temperature derivative (shown in Fig. 3 (a) and (b)).

The maximum and minimum lithiation levels of the electrodes depends on the formation process and electrode voltage limits. The reconstructed electrodes were tested in a half-cell configuration, and thus the influence of the other electrode was removed. When the cell is constructed for the first time, the negative electrode starts completely delithiated (x = 0) and the positive electrode completely lithiated (y = 1).

In the negative electrode, due to the irreversible lithium insertion into the structure at low SoL levels, the electrode does not reach a fully delithiated level after formation cycles. This small shift in the negative electrode is discussed in the Section 4.5 during the electrode balancing process as an offset. Therefore, in this section we assume that all cyclable lithium is removed from the electrode after the initial SEI layer formation so as to establish SoL$_{neg,min}$ = 0. When the SEI layer is created during the first formation cycles or re-created in the reconstructed cell [24], some lithium ions are irreversibly consumed. In the full-cell configuration, this lithium ion consumption affects the positive electrode. However, as a lithium foil is placed against the negative electrode, the lithium source is assumed infinite in this study. Therefore, the maximum lithiation level of the electrode (SoL$_{max,neg}$ = 1) is obtained as the half-cell is cycled in the full lithiation window (between 0.01 and 2 V). This is confirmed by the asymptotic behaviour of the graphite at high lithiation level.

In the positive electrode a complete reversible extraction/insertion of lithium ions is not possible due to the high voltages needed to completely delithiate the layered oxide (common electrolytes are not stable at these voltages) and low stability of those structures [23–25]. As an approximation, this amount of Li ions per formula unit that remain in the cathode structure was calculated with Eq. (2). This corresponds to the non-usable part of the cathode and is calculated with the relationship between the real capacity with respect to the theoretical capacity of the active material of the positive coin cell (SoL$_{pos,min}$). The theoretical electrode capacity is calculated with the Faraday's law, taking into
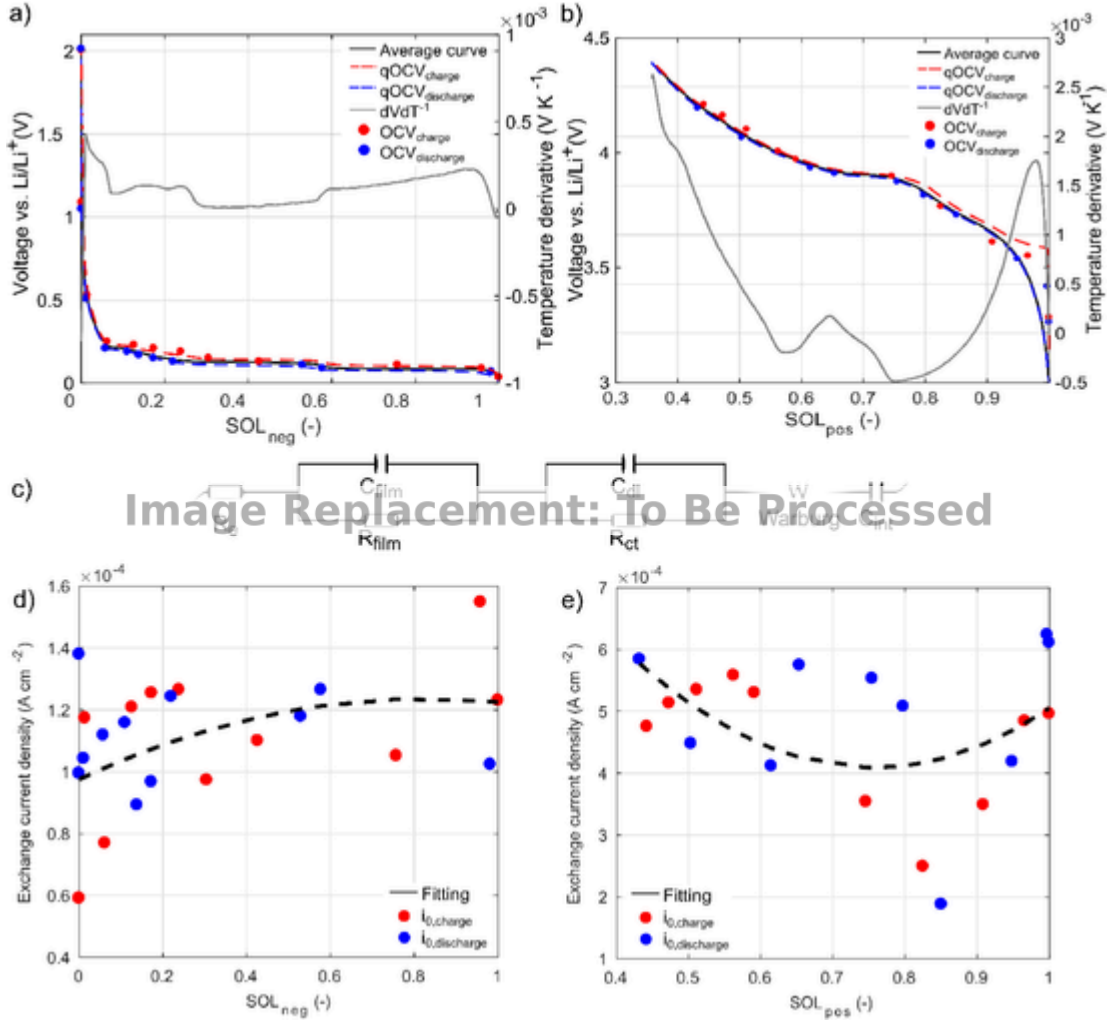
Fig. 3. OCV curve and temperature derivative (dVdT) as a function of SoL (a) negative electrode, (b) positive electrode; (c) Equivalent circuit model used to correlate PEIS measurements with battery internal phenomena; Exchange current density for (d) negative electrode, and (e) positive electrode.

account the active material content, composition of the electrode (described in Section 4.1), and the measured electrode mass of the coin cell (13.0 ± 0.1 mg of the electrode positive mass ($m_{electrode}$)).

$$SoL_{,pos,min} = \frac{1 - C_{pos,coin,exp}}{\left(zFAM_{per} \left(m_{OCelec} - m_{cc} \right) \right) / (3600 M_w)}, \tag{2}$$

where $C_{pos,coin,exp}$ is the maximum experimental coin cell discharge capacity obtained at C/30, z is the number of electrons, F is the Faraday's constant (96,485 (sA mol^{-1}), AM_{per} is the AM percentage, m_{OCelec} is the one side coated electrode mass including current collector, m_{cc} is the mass of the current collector, and M_w the molecular weight of the active material.

As a first approach, the maximum lithiation level (SoL$_{max,pos}$) is assumed to be 1, although re-lithiation does not fully occur in the electrode due to structural changes [44]. All in all, as half-cell configuration is used (lithium foil is placed against the electrode) the lithium source allows an almost full lithium ion insertion within the positive structure.

The interaction between the negative and positive electrode during the formation and usage of the full-cell is explained in Section 4.5.

In addition to the thermodynamic parameters, the potentiostatic electrochemical impedance spectroscopy (PEIS) technique was used to determine the film resistance, charge transfer resistance, and the double layer capacitance for both electrodes. The experiments were per-

formed in half-coin cells at different SoLs and temperatures. The analysed voltages are presented as dots in Fig. 3 (a) and (b). Half-coin cells with maximum voltage amplitude of 10 mV and a frequency range between 11 mHz and 1 MHz were chosen. In this work, the equivalent circuit model proposed in Aurbach et al. [50] was used to correlate measured impedance spectra to different processes occurring inside the battery (shown in Fig. 3 c)). The Butler-Volmer equation (Eq. (3)) was used to calculate the exchange current density (i_0):

$$
\begin{aligned}
I_{ct}(A) &= i_{loc}S \\
&= i_0 S \left[\exp\left(\frac{\alpha_a zF\eta}{RT} \right) - \exp\left(\frac{-\alpha_c zF\eta}{RT} \right) \right],
\end{aligned} \tag{3}
$$

where I_{ct} is the electrode current (A), i_{loc} is the electrode current density (A m^{-2}), S is the effective surface area between the electrode and electrolyte (m^2), α_a and α_c are the anodic and cathodic charge transfer coefficients respectively, R is the universal gas constant, T is the temperature, and η is the overvoltage.

In order to include the active material concentration (c_s) and electrolyte concentration (c_e) dependencies into the model, Eq. (4) is generally used [27]:

$$
\begin{aligned}
i_0 &= F(k_c)^{\alpha_a} \\
&\quad (k_a)^{\alpha_c} \left(1 - c_s/c_{s,max} \right)^{\alpha_a} \left(c_s/c_{s,max} \right)^{\alpha_c} \left(c_e/c_{e,0} \right)^{\alpha_a},
\end{aligned} \tag{4}
$$

where k_a and k_c are the anodic and cathodic reaction constants, respectively.

Considering a charge transfer coefficient of 0.5, those equations could be simplified in Eqs. (5) and (6):

$$I_{ct}(A) = i_0 S \left(\frac{zF\eta}{RT} \right) \tag{5}$$

$$i_0 = Fk \sqrt{\left(1 - c_s/c_{s,max} \right) \left(c_s/c_{s,max} \right) \left(c_e/c_{e,0} \right)} \tag{6}$$

Finally, to obtain the experimental exchange current density, the charge transfer resistance is used. Assuming small overvoltage potentials the following relationship is applied (Eq. (7)):

$$i_0 = \frac{I_{ct}}{\eta} \left(\frac{RT}{zFS} \right) = \frac{1}{R_{ct}} \left(\frac{RT}{zFS} \right). \tag{7}$$

The exchange current density needs to include the effective surface area taking part in the electrochemical reaction. The effective surface area (S) is calculated with the procedure explained in Section 4.4. The effective surface area value is the same for exchange current density and the solid diffusion coefficient calculations, as it corresponds to the effective electrolyte-electrode surface area of the reconstructed coin cells. The values for negative and positive electrodes are 33.99 ± 0.1 and 10.01 ± 0.1 cm^2, respectively. The exchange current density results obtained with this procedure are shown in Fig. 3 (d) and (e).

The obtained exchange current density results show good agreement with the literature. Schmalstieg et at. [27] at 50 % of lithiation obtained a value of $7.43 \ 10^{-4}$ (A cm^{-2}) for graphite, and $5.03 \ 10^{-4}$ (A cm^{-2}) for NMC. Similarly, at the same lithiation level, Ecker et al. [51] reported values of $7.05 \ 10^{-5}$ (A cm^{-2}) and $2.23 \ 10^{-4}$ (A cm^{-2}) for graphite and Li(Ni$_{0.4}$Co$_{0.6}$)O$_2$ electrodes, respectively.

In order to account for the temperature dependence, the exchange current density at three temperatures (278.15, 298.15 and 318.15 K) for 50 % of the SoL range of the electrodes (SoL$_{neg}$ = 0.5 and SoL$_{pos}$ = 0.68) was analysed. The activation energies calculated with Arrhenius law were 11.8 ± 2 kJ mol^{-1} and 9.2 ± 2 kJ mol^{-1} for negative and positive electrodes, respectively.

The average values of the double layer capacitance were 6.746 ± 0.2 (F m^{-2}) and 0.27 ± 0.2 (F m^{-2}), and the average film resistances were 0.014 ± 0.005 (Ω m^2) and 0.178 ± 0.005 (Ω m^2) for the negative and positive electrodes, respectively. Schmalstieg et al. [27] obtained values of 1.47 F m^{-2} and 0.198 F m^{-2} for double layer capacitance for graphite and NMC electrodes, which are in good concordance with our results.

4.3. Transport properties

In this section, the transport properties of the liquid-phase and solid-phase are discussed. The parameters that describe the liquid-phase are the ionic conductivity, the diffusivity, the activity coefficient and the transport number. Together, these four transport properties describe a binary and concentrated electrolyte [7]. They are concentration dependent and cannot be directly determined in commercial cells since the recovered electrolyte is at a specific concentration. For that reason, 1 M and 2 M LiPF$_6$ EC:EMC (50:50 v%) commercial electrolytes were used in this analysis. The ionic conductivity, measured by EIS, is shown in Fig. 4 (a), which is in good agreement with the literature [52].

The transport number was measured with Steady-State Potentiostatic Polarization test (SSPP) using a polarization cell with the reference 1 M electrolyte. The calculations are based on Bruce and Vincent's procedure [52]. A value of 0.28 ± 0.05 was experimentally obtained, which is in good concordance with literature values 0.34 ± 0.07 [17,26].

The diffusion coefficient was calculated with the Einstein relationship assuming a constant transport number and measuring the ionic conductivity [15,22,26] (see Eq. (8)). The activation energies of the conductivity and diffusivity were 14.67 ± 2 kJ mol^{-1} and 17.13 ± 2 kJ mol^{-1}, respectively. In Fig. 4 (b), the values for diffusivity calculated with Einstein relationship are presented.

$$D_e = \frac{\kappa k_B T}{e^2 N_A c_e}, \tag{8}$$

where κ is the ionic conductivity, k_B is the Boltzmann constant, e is the elementary charge, N_A is the Avogadro constant, and c is the lithium concentration of the electrolyte.

In the solid-phase of the electrodes, electronic conductivity and solid diffusion coefficient were determined. The bulk electronic conductivity was determined in the scrapped powder of the electrodes (including AM, binder and additives). The dc-four point probe technique on bulk was used in the discharged state of the cell (0 % SoC). The pycnometry powder density (2.147 ± 0.001 g cm^{-3} and 3.800 ± 0.001 g cm^{-3} for negative and positive electrodes, respectively) was measured in order to estimate sample thickness in electronic conductivity measurements. An average value of 6.6 ± 0.1 (S m^{-1}) and 2.0 ± 0.1 (S m^{-1}) for the negative and positive electrode were recorded, respectively. It is worth mentioning that the effective electronic conductivities (taking Bruggeman exponent and solid volume fraction of the Section 4.4) are 3.9 ± 0.1 and 0.9 ± 0.1 (S m^{-1}) for the negative and positive electrodes, respectively.

In order to obtain measurements that were comparable with the literature, electronic conductivities were also measured in a one sided coated electrode (same as Ecker et al. [23]). The graphite electrode was in the same order of magnitude as values given by Ecker et al. following a similar procedure. The effective conductivity value (the property is measured in the porous electrode) includes the contact resistance between the coating and the current collector. The values obtained in this work were lower than expected; therefore, the measurement methodology should be enhanced. However, there is a high variability of electronic conductivity values in the literature, which vary by several orders of magnitude [25,53,54].

The solid diffusion coefficient (D_s) can be measured using potential-step techniques as a function of the SoC and the temperature. A mixed method combining PITT and PEIS techniques was used taking the methodology from [55]. The equation accounts for morphological $(V_m/zFS)^2$, thermodynamic $(dE_0/dx)^2$ and dynamic $\left(1/\sqrt{2}A_w \right)^2$ factors (Eq. (9)):

$$D_s = \left(\frac{V_m}{zFS} \right)^2 \left(\frac{dE_0}{dx} \right)^2 \left(\frac{1}{\sqrt{2}A_w} \right)^2, \tag{9}$$

where V_m is the molar volume of the insertion material, dE_0/dx is the equilibrium potential-concentration profile of the material (from PITT), and A_w is the Warburg coefficient (from PEIS).

The solid diffusion coefficient results for positive and negative electrodes are presented in Fig. 4 (c) and (d).

4.4. Parameters related to the porous structures and adjustable design parameters

The porous structure is defined during the mixing, coating, drying and calendering steps of the fabrication process of the batteries, and changes during charge-discharge processes due to the expansion/contraction of the materials [56]. In this paper, only the full-cell discharged state is characterised.

First of all, the raw materials (NCA, LCO, graphite) shape and size were characterised. These properties are defined during the synthesis
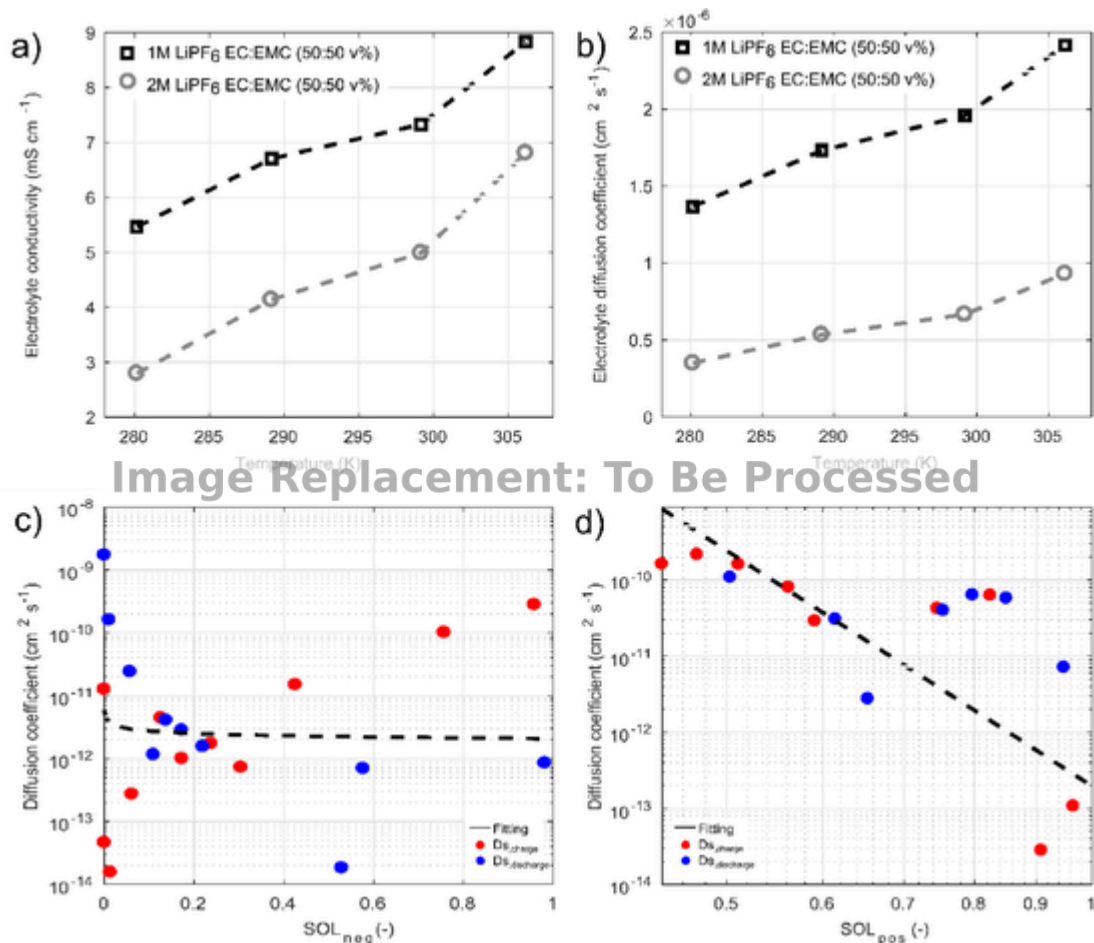
Fig. 4. (a) Ionic conductivity of the reference 1 and 2 M LP50 commercial electrolytes, (b) electrolyte diffusion coefficient, (c) solid diffusion coefficient of the negative electrode and (d) solid diffusion coefficient of the positive electrode.

process and are critical to form the porous structure of the electrodes [57]. The effective particle diameter was calculated based on dynamic light scattering (DLS) measurements, and compared to SEM image processing results. In Fig. 5 (a) and (b) the results obtained with DLS are presented. Samples were analysed in powder after a heat treatment to remove the binder. This technique was used to obtain a particle size distribution of the analysed compounds. Moreover, SEM images were treated to obtain an average particle size of the electrodes and compared with the DLS measured effective particle diameter (see Fig. S3).

The model assumes uniform sized and spherical particles in both electrodes, which affects the accuracy of the results. In DLS results, an effective particle diameter (Dv 50) of 13.1 ± 1.5 μm and 7.0 ± 0.6 μm for the negative and positive electrodes respectively, was calculated. With SEM analysis two different distributions corresponding to the previously identified blended material in the positive were measured in 2D electrode slices. The averaged particle diameter with SEM image post-processing were 13.7 μm for the graphite, 9.2 μm for the NCA, and 10.0 μm for the LCO active materials.

In Fig. 5 (c) the cross-section image of the negative electrode is presented, showing a flake-like shape (commonly seen in graphite electrodes). In Figs. 2 (c) and 5 (d) the SEM images of the positive electrode are presented, in which spherical particle shape is seen.

The geometrical parameters of this specific battery are given in Table 1. The thicknesses of the electrodes and the cross-sectional area (based on electrode width and length) are the parameters used in the P2D model. The cross-sectional area of the cell is 23.15 ± 0.1 cm^2, which corresponds to the positive electrode. The negative is larger than

the positive electrode (1 cm^2 bigger) in order to ensure the whole positive electrode utilization, and reduce the dendrite formation risk [58]. The porous structure related parameters are defined during the electrode fabrication process (porosity, solid volume fraction, tortuosity/Bruggeman coefficient and specific surface area) which affect to the final performance of the cell.

In order to calculate the electrode coating porosity (ε_e) mercury porosimetry measurements were performed. In these experiments bulk and skeletal densities are calculated and corrected, so as to obtain the average porosity. As the P2D model does not account for pore size distribution, the average porosity value was used in the simulations (Eq. (10)).

$$\varepsilon_e = 100 \left(1 - \frac{\rho_{bulk,coating,Hg}}{\rho_{skeletal,coating,Hg}} \right), \tag{10}$$

where $\rho_{bulk,coating,Hg}$ is the two sided coating mercury density (bulk density) and $\rho_{skeletal,coating,Hg}$ is the two sided coating mercury density (skeletal density).

The skeletal density and electrode coating bulk density were corrected in accordance with Froboese et al. [59] (Eq. (11)) with the proposed correction by given sample area and mercury mass replacement.

$$\varepsilon_s = \frac{\left(V_{p,HL} - V_{p,LL} \right) \rho_{Hg}}{m_{pen,Hg} - \left[\left(m_{pen,Hg,sam} - m_{cc} + \left(\rho_{Hg} M L_{cc} A_{cc} \right) / \rho_{cc} \right) - m_{coating} \right]}, \tag{11}$$

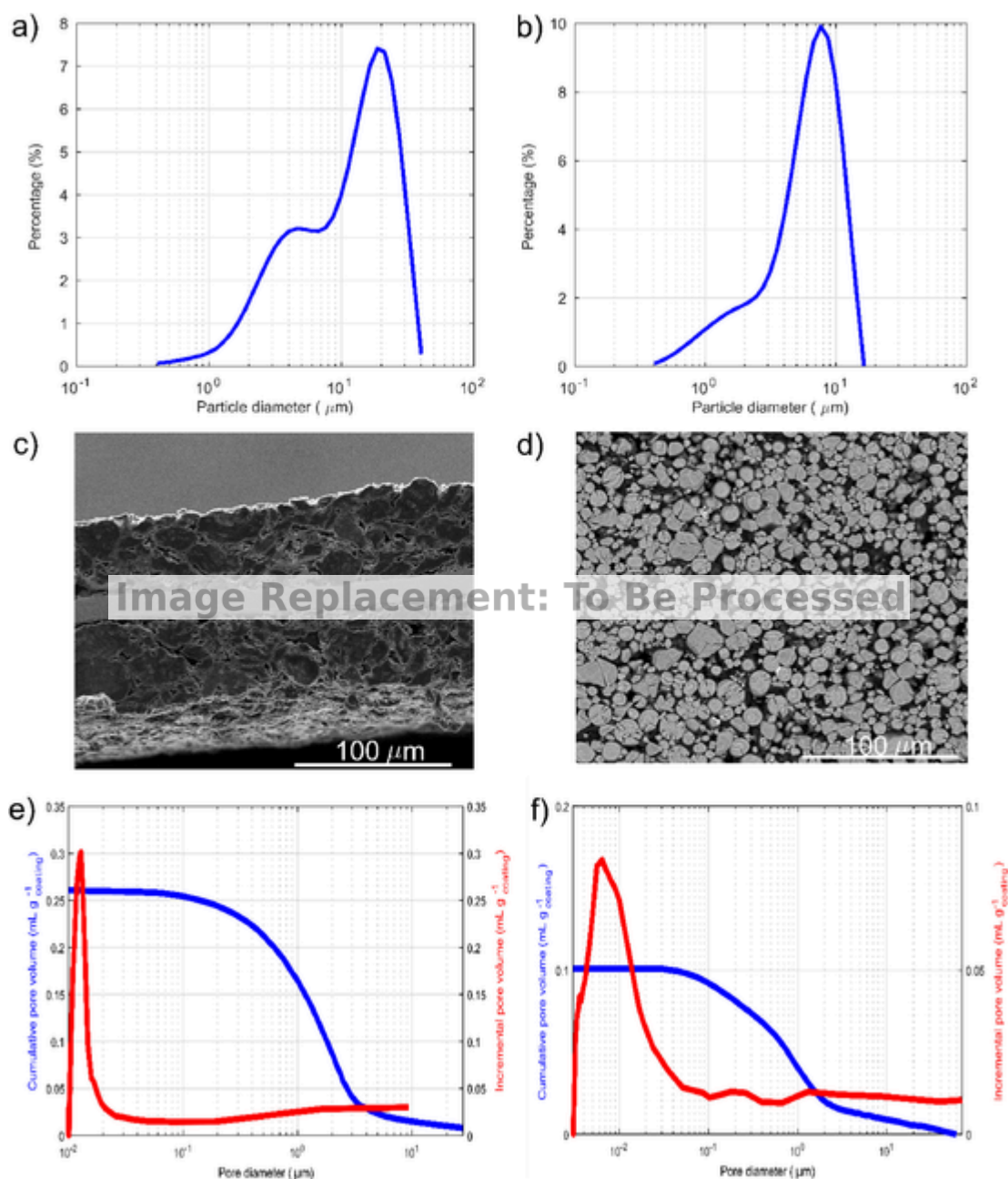where $V_{p,HL}$ is the maximum intruded mercury volume at the lowest

Fig. 5. Particle size distribution for (a) negative electrode and (b) positive electrode; (c) SEM cross-section image of the negative electrode (prepared by ion milling) (d) SEM surface image of the positive electrode; Mercury porosimetry results for (e) Negative electrode, and (f) Positive electrode.

Table 1
Summary of the porous structure parameters for the electrodes and separator.

Parameter	Positive electrode	Negative electrode	Separator
W (cm)	3.8 ± 0.1	3.9 ± 0.1	156.4 ± 0.1
H (cm)	6.1 ± 0.1	6.2 ± 0.1	6.5 ± 0.1
L (μm) [*1]	32.2 ± 0.5	49.8 ± 0.5	13.8 ± 0.5
R_s (μm)	6.55 ± 0.7	3.5 ± 0.3	-
ε_e (-)	0.27095 ± 0.00005	0.22193 ± 0.00005	0.51 ± 0.00005
ε_s (-)	0.600 ± 0.00005	0.704 ± 0.00005	0.49 ± 0.00005
a_s (m^2 m^{-3})	5.11 ± 0.1 10^5	3.22 ± 0.1 10^5	-
p	1.50 ± 0.001	1.46 ± 0.001	1.38 ± 0.001

[*1] One side coating. Only the coated thickness is presented, without current collector.

considered pore diameter (0.01 nm), $V_{p,LL}$ is the minimum intruded mercury volume at the highest considered pore diameter (based on Dv90 of the DLS measurements), ρ_{Hg} is the mercury density, $m_{pen,Hg}$ is the weight of penetrometer and mercury, $m_{pen,Hg,sam}$ is the assembly weight (penetrometer, mercury and sample), ML_{cc} is the mass loading of the current collector, and A_{cc} is the area of the current collector.

In this case, bulk densities were 1.085 ± 0.001 g cm^{-3} and 2.468 ± 0.001 g cm^{-3} and skeletal densities were 1.489 ± 0.001 g cm^{-3} and 3.0454 ± 0.001 g cm^{-3} for the negative and positive electrodes, respectively. Combining both results, 27.095 ± 0.005 % porosity was defined for the negative electrode and 22.193 ± 0.005 % for the positive electrode. The pore size distributions obtained by mercury porosimetry are presented in Fig. 5 (e) and (f), and are in good concordance with literature [25].

In addition to the liquid-volume fraction or coating porosity (ε_e) within the porous electrode, the solid-volume fraction (ε_s) need to be defined. To this end, the inactive part of the electrodes (binder and additives) should be estimated. Apart from the inert materials which form the composite solid matrix, some parts of the active material do not react and the solid volume fraction should be corrected adding the contribution of the non-electrochemically active volumes. The used values for the model are presented in Table 1. Therefore, the solid-volume fraction of the material can be calculated as follows (Eq. (12)):

$$\varepsilon_s = 1 - \varepsilon_e - \varepsilon_{non-act}, \tag{12}$$

where $\varepsilon_{non-act}$ corresponds to the non-electrochemically active volumes (binder, additives, closed pores etc.).

To calculate the non-electrochemically active volume of the material, Eqs. (2) and (12) should be combined (Eq. (13)). This relationship is then used in the electrochemical model, allowing the coherence between experimentally obtained results and simulations.

$$\varepsilon_{non-act} = 1 - \varepsilon_e - \left(\frac{C_{pouch,\exp}}{C_{pouch,th}} \right), \tag{13}$$

where $C_{pouch,\exp}$ is the experimental and $C_{pouch,th}$ is the theoretical pouch cell capacity.

Different methods to calculate the specific surface area between the active material and the electrolyte can be found in the literature [7,22,26,56]. In all the cases, the assumption made during the experimental parameter measurement and simulations should be the same so as to have the ability to recalculate the area-related variables in the model [54]. Assuming uniform size and spherical particles, the approximation presented in Eq. (14) can be applied [10]:

$$a_s = \varepsilon_s \frac{4\pi R_s^2}{(4/3)\,\pi R_s^3} = \frac{3\varepsilon_s}{R_s}. \tag{14}$$

Moreover, the surface area (used for exchange current density and solid diffusion coefficient calculations) is calculated as in Eq. (15) [27] in which a value of 33.99 ± 0.1 and 10.01 ± 0.1 cm^2 were obtained for negative and positive electrodes, respectively.

$$S_{coin} = \frac{3V_{coin}\varepsilon_s}{R_s} = \frac{3A_{coin}L\varepsilon_s}{R_s}. \tag{15}$$

Finally, the tortuosity of the electrodes is defined. The tortuosity is defined as the ratio between the shortest and real path of the ion to diffuse in a porous media (Eq. (16) [59]).

$$\tau = \frac{L}{L_0} \tag{16}$$

In this paper, the pore tortuosity was analysed by means of Carniglia's equation (Eq. (17) [60]), in which Fick's first law is used to describe fluid diffusion in cylindrical pores. The equation validity range for both electrodes was confirmed ($0.05 \le V_{p,c}\rho_{coating,Hg} \le 0.95$).

$$\tau = \left(2.23 - 1.13V_{p,c}\rho_{coating,Hg}\right), \tag{17}$$

where $V_{p,c}$ is the intruded mercury volume per electrode coating mass.

The Bruggeman relationship is widely used in the literature to relate the tortuosity with the volume fraction (Eq. (18) [4,7]). The extended Bruggeman relationship was applied and the results are given in Table 1.

$$p = 1 - \log_{\varepsilon_e}(\tau) \tag{18}$$

Obtaining a value of 1.50 ± 0.001 and 1.46 ± 0.001 for the Bruggeman exponents, which is in good concordance with the literature [61].

In order to determine the separator parameters (porosity, tortuosity and Bruggeman exponent) the methodology that is explained in Arora et al. [31] was followed. In this method, the porosity of the sample is calculated based on the measured mass and geometrical volume of the separator compared to the true density of the separator (measured by helium pycnometry). The tortuosity of the separator was calculated by means of the difference between the electrolyte resistivity and the separator effective resistivity. Therefore, the resistivity of the separator sample impregnated in electrolyte using the reference 1 M LP50 electrolyte is measured (Eq. (19) [31]):

$$\frac{\rho_s}{\rho_e} = \frac{\tau^2}{\varepsilon_e}, \tag{19}$$

where ρ_s is the specific resistivity of the separator saturated with electrolyte, and ρ_e is the specific resistivity of the electrolyte.

4.5. From components to full-cell: cell internal configuration and electrode balancing

The cell internal configuration is shown in Fig. 6 (a). It was assembled with 18 layers of double side coated negative electrodes, 17 layers of double side coated positive electrodes, and 2 single side coated positive electrodes. A Z-folding configuration was used to place the separator in between the electrodes and the cell was divided in two subcells.

The internal configuration is directly related to electrode balancing as the number and size of the electrodes determines the final cell capacity. Electrode balancing is a key process in the fabrication of batteries. After the step of cell assembly, formation cycles are performed to create the SEI layer and activate the cell. When the cell is charged for the first time, lithium ions are deinserted from the positive electrode and inserted in the negative electrode. In the first discharge process lithium ions are deinserted from the negative electrode and reinserted in the positive electrode. Note that after the first full cycle the positive electrode lithiation is y < 1, due to the SEI formation and negative electrode irreversibility (lithium ions get trapped in the electrode structure, resulting in a decrease of the lithium inventory f_{loss}). One or more cycles need to be performed so as to form a stable SEI that provides the needed stability of the cell. In the case of commercial cells, information about formation cycles was not available.

In the literature, different approaches for electrode balancing are found [16,18,24,27,49]. In all these cases half coin cell reconstruction is necessary to study negative and positive electrodes separately. In the next paragraphs, the methodology that was implemented for electrode balancing is presented. From the electrode balancing, the operational limits of the electrodes ($SOL_{neg,0}$, $SOL_{neg,100}$, $SOL_{pos,0}$ and $SOL_{pos,100}$) as well as the excess of negative electrode (f_{excess}), and the loss of lithium inventory in the positive electrode (f_{loss}) due to the first formation cycles were obtained. A graphic explanation of the electrode balancing parameters and the interaction between them is presented in Fig. 6 (b).

In order to determine the full electrode balancing, in addition to electrode qOCVs (see Section 4.2), the qOCV curves at C/30 and 298.15 K from full coin and full pouch cells were experimentally obtained. First, the experimental qOCV tests were scaled from coin cell level to pouch cell level using $scale_{coinTOpouch}$ scaling factor (Eq. (20)):

$$Q_{pouch} = Q_{coin,FC}\,scale_{coinTOpouch} \tag{20}$$

To correct the small experimental deviations that can arise due to the set-up of the experiments, a correction factor was applied separately to each electrode. These correction factors are understood to be a small variation of less than 10 % of the real capacity, which could
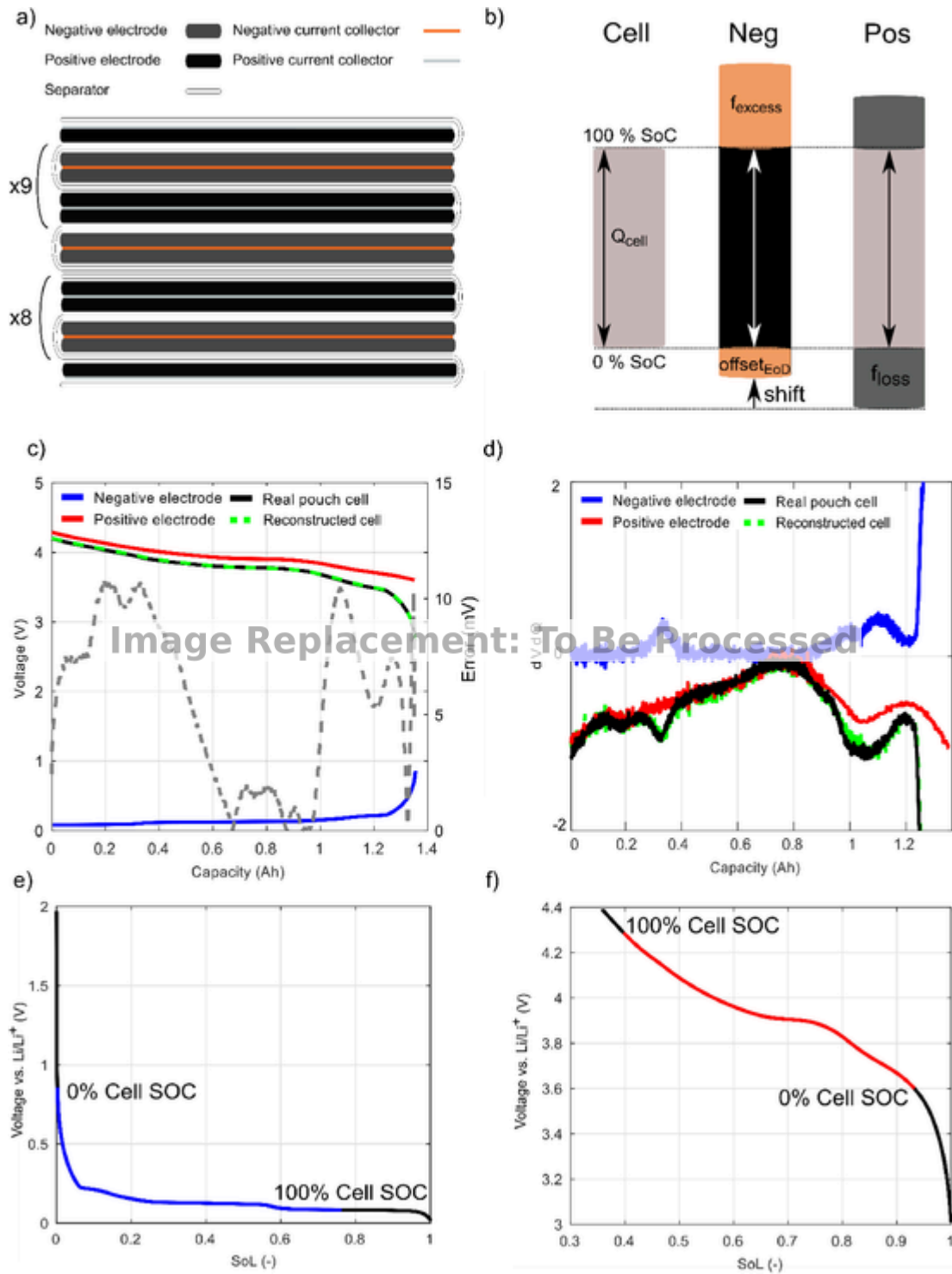
Fig. 6. (a) Cell internal configuration; (b) Graphic representation of the electrode utilization range; (c) Pouch cell, reconstructed cell, negative and positive electrode voltage responses as a function of the cell capacity; (d) dVdQ plot of the pouch cell, reconstructed cell, negative and positive electrodes. Equilibrium potential curve and electrode utilization range for (e) negative electrode (blue) and (f) positive electrode (red) (For interpretation of the references to color in this figure legend, the reader is referred to the web version of this article.).

come from coin cell reconstruction process (see Eq. (21)).

$$Q_{pouch} = Q_{neg,coin} scale_{coinTOpouch} scale_{neg,corr}$$
$$= Q_{pos,coin} scale_{coinTOpouch} scale_{pos,corr}$$

(21)

Taking as a reference the maximum and minimum lithiation states of the materials ($SOL_{neg,max}$, $SOL_{neg,min}$, $SOL_{pos,max}$ and $SOL_{pos,min}$) of Section 4.2, the excess of negative electrode active material (f_{excess})

was determined by means of the following relationship (Eq. (22)).

$$f_{excess} = 1 - \left(\left(SOL_{neg,max} - S \right. \right.$$
$$OL_{neg,min} \right) \left(\frac{\max\left(Q_{pouch}\right)}{\max\left(Q_{coin,FC}\right)} \right) scal \tag{22}$$
$$\left. e_{coinTOpouch}\, scale_{neg,corr} \right).$$

Then, the negative electrode lithiation states at 0 and 100 % of SoC of the pouch cell were calculated (Eqs. (23) and (24)). As a starting point, $offset_{EoD}$, which corresponds to the lithium trapped irreversibly in the negative electrode structure at low lithiation levels, was set to zero.

$$SOL_{neg,100} = SOL_{neg,max} - f_{excess} + offse$$

$$t_{EoD}(23) SOL_{neg,0} = SOL_{neg,100} - \left(\left(S \right. \right.$$
$$OL_{neg,max} - S$$
$$OL_{neg,min} \right) \left(\frac{\max\left(Q_{pouch}\right)}{\max\left(Q_{coin,FC}\right)} \right) scal \tag{24}$$
$$\left. e_{coinTOpouch}\, scale_{neg,corr} \right)$$

Once the f_{excess} was determined, the voltage difference between the full pouch cell and negative electrode at 100 % SoC ($SOL_{neg,100}$) was used to first calculate the $SOL_{pos,100}$, and thus, calculate the initial f_{loss} (Eq. (25)). This parameter was updated iteratively during the electrode balancing process.

$$f_{loss} = 1 - \left(SOL_{pos,100} + \left(SOL_{pos,max} - S \right. \right.$$
$$OL_{pos,min} \right) \left(\frac{\max\left(Q_{pouch}\right)}{\max\left(Q_{pos,coin}\right)} \right) scal \tag{25}$$
$$\left. e_{coinTOpouch}\, scale_{pos,corr} \right)$$

Finally, the lithiation states at 0 % and 100 % of SoC of the cell for the positive electrode are defined as (Eqs. (26) and (27)).

$$SOL_{pos,0} = SOL_{pos,max} - f_{loss} \tag{26}$$

$$SOL_{pos,100} = SOL_{pos,0} - \left(\left(SOL_{pos,max} - S \right. \right.$$
$$OL_{pos,min} \right) \left(\frac{\max\left(Q_{pouch}\right)}{\max\left(Q_{pos,coin}\right)} \right) scal \tag{27}$$
$$\left. e_{coinTOpouch}\, scale_{pos,corr} \right)$$

In Fig. 7 (c) the experimental and reconstructed cell voltage, the negative and positive electrode voltages, and the error between the fitting and experimental voltage are presented. A maximum error of 10.75 mV or 0.36 %, and a mean error of less than 5.69 mV or 0.15 % is reported.

In Fig. 7 (d), the dVdQ plot of experimental and reconstructed curves is shown. A $scale_{pos,corr}$ of 0.98 and $scale_{neg,corr}$ of 0.93 were used to correct the reconstructed electrode balancing curves to fit experimental pouch cell data. In fact, the dVdQ peaks can be related to voltage plateaus of the graphite during coexisting phases and phase transitions. The positive electrode dVdQ are related to the material phase changes [30].

Finally, the OCV curve as a function of the lithium content of the electrodes and the utilization range of the full-cell is shown in Fig. 7 (e) and (f). The positive electrode utilization range is between 0.40 and 0.93 SoL, and negative utilization range between 0.002 and 0.76 of SoL, which is in good concordance with the literature [23,27,49]. In addition, a f_{excess} of 0.24 and f_{loss} of 0.07 was obtained. It is worth mentioning that, as the positive electrode is a blended material composed of LCO and NCA, the x-axis of Fig. 6 (f) was obtained assuming a ratio between materials of 50 % and assuming that the material dynamics of both materials are equal.

4.6. Model response evaluation

The model response evaluation is used as a proof of the validity of the parameter measurement methodology. In this work, model responses in a wide operation range were compared against experimental measurements of the analysed device, giving a reliable view of the accuracy of the parameters. Validation tests at the full pouch cell level, which include galvanostatic charge-discharge cycles at different temperatures and currents, pulse tests (HPPC procedure) at different SoCs, and PEIS tests were performed.

First of all, the time-domain model was used for electrode balancing verification and correct implementation of all the parameters (at low current rate (C/30) and 25°C) (see Fig. 7(a). The maximum error obtained in the discharge curve C/30 and 25°C was less than 1% of capacity (see Fig. 7(b)). Once the model parameters and responses were confirmed at low current rates at 25°C, the dynamic response of the model needed to be assessed. First, galvanostatic cycles were checked, as shown in Fig. 7(c) and the error Fig. 7(d). In Table 2 the maximum capacity deviation for different conditions (5, 25 and 45 °C and galvanostatic charge and discharges) are presented.

The maximum voltage deviation was found at high current rates and high temperatures. In Fig. 7 (e) and (f) the lithium concentration inside particles and electrolyte are presented for a 1C discharge, respectively. These internal variables give an insight into whether the active materials or the electrolyte are the limiting factors of the discharges. At high rates, the solid diffusion coefficient and the reaction rate are key parameters, which limit the fast charging ability of electrodes. The initial concentration of the electrolyte is sufficient to prevent depletion of the lithium ions in the parts closest to the current collectors, in which the electrolyte concentration is lower.

Secondly, the impedance spectroscopy test showed greater deviations than the other tests (Fig. 7 (g)). A second semi-circle is appreciable in the experimental curve. This could be attributed to the second phase of the positive material. Nevertheless, the average exchange current density, electrode capacitance, electronic conductivity and solid diffusion coefficient seems to be in good correlation with the literature (in terms of the order of magnitude).

The final step was to employ the HPPC test. A good correlation between the simulations and the experimental pulses are seen in Fig. 7 (h) for different SoCs. As was the case for the previous step, the main differences arising from this test could also be due to the blend positive material.

Usually, the model validation ends with non-invasive test characterisation. However, invasive tests can provide relevant information about the lithiation state of the materials and electrode balancing.

A T-cell type three-electrode cell set-up is used for this purpose to evaluate the voltage evolution of each electrode separately. With this set-up, the voltage contribution of each electrode to the overall cell potential is experimentally obtained. In Fig. 8(a) the experimental-numerical comparison of the electrodes potential is presented, showing
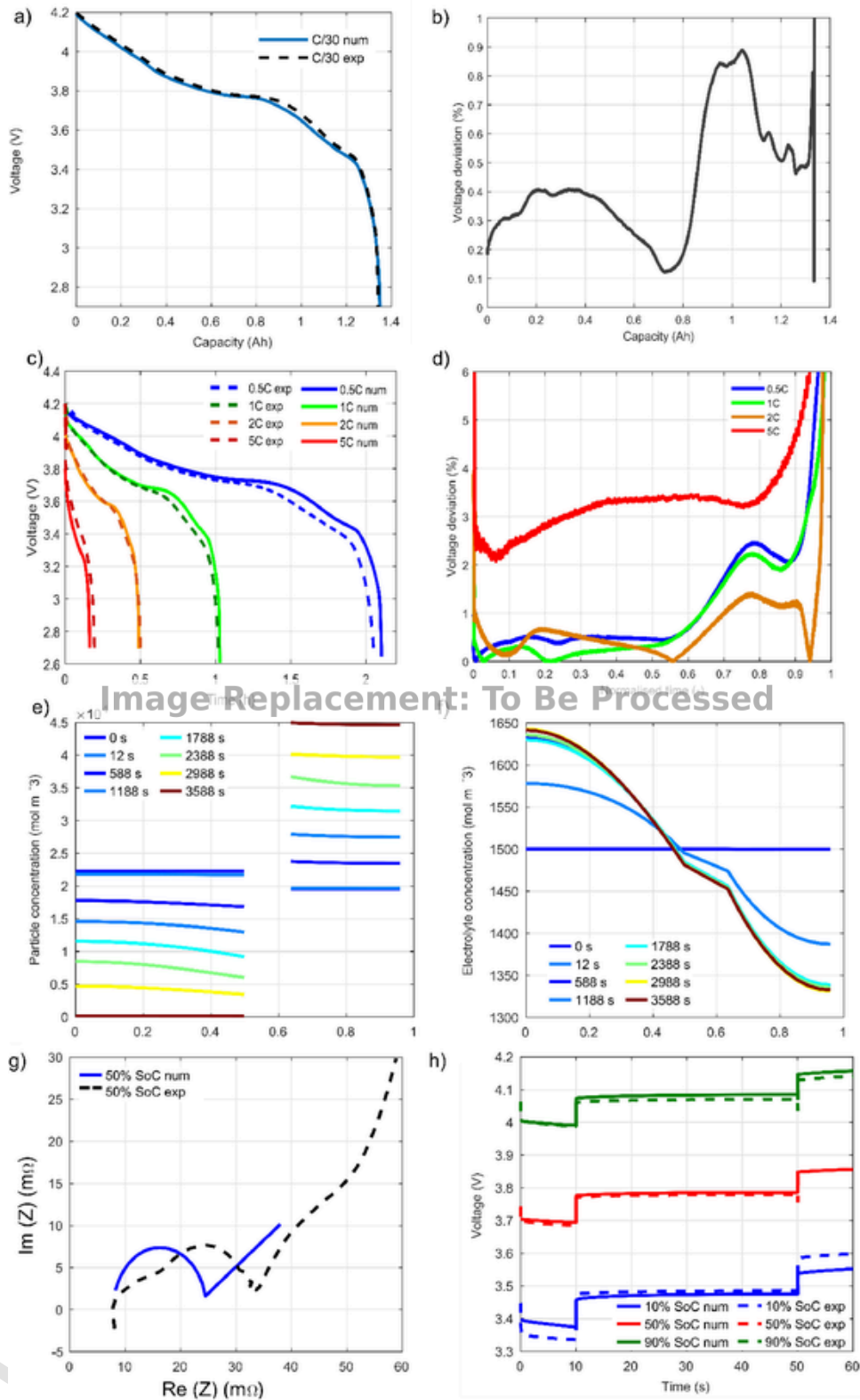
Fig. 7. (a) Experimental C/30 curve vs C/30 simulation at 25 ℃; (b) Voltage deviation between experimental and numerical C/30 curves; (c) Galvanostatic discharges at different current rates at 25℃; (d) Voltage deviation between experimental and numerical galvanostatic discharge curves at 25℃; (e) State of lithiation of the electrodes for a 1C discharge at 25 ℃; (f) Electrolyte concentration for a 1C discharge at 25 ℃; (g) PEIS at 50 % of SoC and 25 ℃; (h) HPPC pulses at different SoCs for 25 ℃.

Table 2
Experimental and numerical maximum capacity deviations(%).

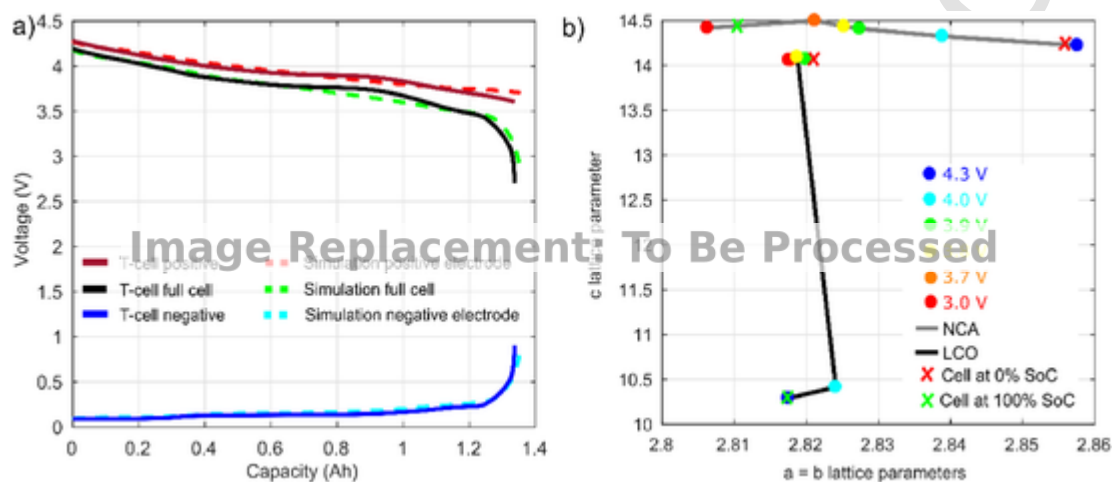| Temperature	5 °C		25 °C		45 °C	
C-rate	Discharge	Charge	Discharge	Charge	Discharge	Charge
0.5C	0.34	3.42	2.66	6.50	5.79	20.46
1C	0.92	0.55	1.05	4.88	7.23	25.53
2C	4.46	5.11	1.97	0.22	5.52	36.42
5C	19.26	-	15.39	-	5.41	-

Fig. 8. (a) Comparison of the voltage evolution of the three electrode T-cell at 25°C and C/10 and the P2D model; (b) Lattice parameters of the positive electrode (two phase material) analysed with LeBail profile matching.

good agreement between experimental T-cell electrode balancing and the methodology presented in Section 4.5.

Additionally, the solid lithium content of the positive active materials predicted by the model were obtained experimentally by means of *ex-situ* XRD measurements at different electrode voltages (Fig. 8 (b)), so as to give insight into the understanding of blended materials. A calibration curve (dots and lines) was determined to experimentally obtain the starting and ending SoLs (crosses) of the active materials based on the lattice parameters. At 100 % of SoC, the lithiation level of LCO phase is almost 1, whereas the NCA phase is lower. This is in good correlation with literature [62]. Morover, at 0 % of SoC, the lattice parameters are closed to 4.3 V which is the expected results from Fig. 8 (a). XRD diffractograms of the calibration curve are plotted in Fig. S4 for negative and positive electrodes. This calibration curve could also be used for ageing mechanism study [30].

The consideration of uncertainty of model parameters in a real application is a non-trivial issue [63–66]. Not only parameter uncertainty (cell-to-cell variability and measurement repeatability), but also assumptions taken from the electrochemical model itself (because equations does not describe the desired phenomena 100% accurately) should also be discussed. Due to these reasons when considering a real system, the uncertainties and inaccuracies need to be somehow handled. Different types of methods are reported in the literature, but Kalman filters are the most extensively used method [67]. These feedback-based algorithms seek to somehow tune the model to fit the observed behaviour, based on the assumption that the inaccuracies and uncertainties follow a statistic distribution. Thus, the errors introduced by the model (where both, parametric and model error) can be contemplated. These filters are able to give a more accurate prediction based on the expectancy of the desired prediction, but more important, are able to give confidence boundaries. These boundaries will give insight on how precise the prediction could be, and allow to adopt conservative or optimistic predictions, based on use of those.

5. Conclusions

Obtaining a consistent set of parameters is essential to effectively evaluate battery performance by means of electrochemical modelling. Therefore, a complete physico-chemical methodology to measure all the necessary parameters for a pseudo-two-dimensional (P2D) electrochemical model is provided. In this work, a guideline for classifying and selection of the experimental techniques to measure model parameters is proposed. Several specific contributions were also proposed from the previous methodologies which are: (1) The identification of a blend positive electrode composed of LCO and NCA based on EDS mapping; (2) The ratio determination between LCO and NCA based on ICP-OES measurements; (3) The estimation of the formulation of both electrodes based on TGA measurements; (4) The electrolyte concentration estimation, even if no liquid was recovered, based on weighting and volume measurements; (5) The electrolyte composition determination based on GC-MS and NMR measurements; (6) The elucidation of the coherence between the experimental and simulated the specific surface area; (7) The measurement of separator properties; and (8) Electrode balancing determination based on reconstructed half and full cells and the commercial full-cell measurements.

The response to different tests performed in pouch cells were compared with model predictions in order to determine the accuracy of the parameter measurement methodology. This methodology was tested at the beginning of life of a commercial battery although it is also valid for ageing evolution analysis.

To validate the methodology, first, galvanostatic charge-discharge processes at low current rates and 25 °C were selected for balancing proof determination. The composition and ratio of active materials was determined by means of XRD and TGA, which reduce the theoretical capacity calculation deviation and allow us to identify that the positive electrode has a blend composition of LCO and NCA. Electrode balancing was assessed with a method accounting for lithium loss of the posi-

tive electrode during the SEI formation, and negative excess of capacity for lithium plating prevention. A maximum voltage deviation of 10.75 mV or 0.36% was reported for this methodology. The experimental-simulation comparison is in good agreement at low galvanostatic current rates.

Then, galvanostatic tests at different current rates and temperatures were compared to voltage predictions. The maximum voltage deviation was found at high current rates and high temperatures. Furthermore, to check the dynamic behaviour of the cells and the accuracy of thermo-dynamic, kinetic and transport parameters HPPC pulse testing and impedance spectroscopy tests were employed. Good correlation between experimental and numerical results were obtained in pulse tests. Larger deviations are presented in impedance spectra which could be attributed to the positive blend material, electrolyte uncertainty or oversimplification of the model. It is worth mentioning that, although real porous structures present particle and pore size distributions, the model only accounts for averaged porous properties. In addition, the model assumes spherical particles, although graphite is flake-shaped. The model accuracy could be enhanced adding complex 3D structures, but this leads to an increase in computational time.

Internal variables of the model (electrode potentials, electrolyte potential, electrolyte concentration and active material lithiation) provide valuable information about the limitations of the cell at the analysed conditions. At high rates, the solid diffusion coefficient and the reaction rate are key parameters, which limit the fast charging ability of electrodes. Moreover, at 1C discharge, the initial concentration of the electrolyte is sufficient to prevent depletion of the lithium ions in the parts closest to the current collectors, in which the electrolyte concentration is lower. The electrolyte salt and solvent ratio were determined by means of NMR and GC-MS, so as to perform all the characterisation tests with a similar electrolyte. However, the low amount of electrolyte of the commercial cells available for these tests hindered accurate electrolyte characterization, which could affect into the model predictions.

Finally, invasive tests (three electrode cell and *ex-situ* XRD measurements) were performed to provide more information about the internal variables of the cell. The three-electrode experimental cell is in good agreement with the numerical results of the cell. This validation confirms the model ability to monitor negative electrode potential (which is useful to study lithium plating). Moreover, a calibration curve of the lattice parameters of the positive active materials by means of *ex-situ* XRD allow us to decouple experimentally the contribution of each blend material phase at different analysed voltages. These calibration curves were used to place the cell maximum and minimum SoCs (0 % SoC and 100 % SoC of the pouch cells), and thus providing additional information of the lithiation evolution of both materials (LCO and NCA).

Parameters estimation uncertainty in terms of cell-to-cell variation, even if crucial to keep the estimations accuracy, is a difficult task to undertake due to the difficulty of measuring large sets of samples. Due to the laboratory time consuming experiments, from a practical point of view is not feasible to conduct such analysis to obtain a Gaussian distribution to assess the maximum parametric variability of cells. The maximum dispersion between tested cells at full cell level were found to be 1.328 ± 0.025 Ah and 38.8 ± 9 mΩ in capacity and resistance, respectively. Those variabilities in the effects of cell performance (capacity and internal resistance) can be linked to the contribution of each parameter, not only at the beginning of life of the batteries, but also during operation until the end of life. For that, Kalman filters are a good alternative to deal with cell-to-cell variation to take into account the parametric and model uncertainties. Prediction errors can be improved to some extent when applying these statistic-based algorithms. Furthermore, uncertainty boundaries are provided, so confidence boundaries can be obtained to cope with model inaccuracies, sensing errors and parameters induced uncertainties.

Moreover, to determine the variability of each parameter, the physico-chemical parameter measurement procedure proposed in this research could be combined with parameter identification methods. This mixed methods (combinations between experimental and optimisations) could give an insight about the parametric variability between cells and thus give the dispersion between cells.

Uncited references

[33,34]

CRediT author statement

L.Oca: Conceptualization, Methodology, Investigation, Software, Validation, Original draft preparation; E. Miguel: Conceptualization, Validation, Writing- Reviewing and Editing; E. Agirrezabala: Software; A. Herran: Methodology, Investigation; E. Gucciardi: Methodology, Investigation, Writing- Reviewing and Editing; L. Otaegui: Validation, Writing-Reviewing and Editing; E. Bekaert: Writing- Reviewing and Editing; A. Villaverde: Writing- Reviewing and Editing; U. Iraola: Supervision, Writing- Reviewing and Editing

Declaration of Competing Interest

The authors declare that they have no known competing financial interests or personal relationships that could have appeared to influence the work reported in this paper.

Supplementary materials

Supplementary material associated with this article can be found, in the online version, at doi:10.1016/j.electacta.2021.138287.

Appendix A

The characterization techniques and equipment used in this paper are presented in the Table A1.

List of symbols

Table 1. Pseudo-two dimensional model parameters: symbols and description.

Symbol	Unit	Description
Comp$_{sep}$	-	Separator material
R$_{solv}$	-	Ratio between electrolyte solvents
Comp$_{salt}$	-	Electrolyte salt identification
Comp$_{AM}$	-	Active material composition
M_w	kg mol^{-1}	Molecular weight of the active material
AM	%	Active material content
$c_{e,0}$	mol m^{-3}	Initial electrolyte concentration
U_{ocp}	V	Electrode open-circuit potential
dU_{ocp}/dT	V K^{-1}	Reversible entropy of active electrode material
$c_{s,max}$	mol m^{-3}	Maximum solid lithium concentration
θ_0	1	Minimum electrode state of lithiation (SoL) (stoichiometric value)

Table A1
Characterization techniques: character, acronym, full name and used equipment.

Character. Acronym	Full name of the technique	Equipment used in this paper
a. FTIR	Fourier Transform Infrared spectroscopy	Vertex70. Bruker
b. GC-MS	Gas Chromatography–Mass Spectrometry	Perkin Elmer Mass Spectrometer. Clarus SQ8T
c. NMR	Nuclear Magnetic Resonance spectroscopy	H NMR Bruker Avance III 300 MHz
d. XRD	X-Ray powder Diffraction	Bruker D8 Discover
e. ICP-OES	Inductively Coupled Plasma Optical Emission Spectrometry	Ultima 2, ICP optical emission spectrometer. Horiba Scientific
f. TGA	Thermogravimetric Analysis	TG 209 Libra. Netzsch
g. DLS	Dynamic Light Scattering	Mastersizer 3000. Malvern
h. OCV/cycling	Open Circuit Voltage, cycling	BioLogic VMP3 and Gamry Interface 1000
i. PEIS	Potentiostatic Electrochemical Impedance Spectroscopy	BioLogic VMP3
j. SSPP	Steady-State Potentiostatic Polarization	BioLogic VMP3
k. PITT	Potentiostatic/Galvanostatic Intermittent Titration Technique	BioLogic VMP3
l. Micrometer/ balance	Micrometer and precision balance	Mitutoyo IP65 and Practum: Sartorius
m. SEM-EDS	Scanning Electron Microscopy and Energy Dispersive X-Ray spectroscopy	FEI Quanta 200 FEG-SEM
n. Pycnometry	Helium pycnometer	Accupyc II 1340. Micromeritics
o. Hg-porosimetry	Mercury intrusion porosimetry	Autopore V, Micromeritics

θ_{100}	1	Maximum electrode state of lithiation (SoL) (stoichiometric v
i_0	A m^{-2}	Exchange current density
$E_{act,i0}$	J mol^{-1}	Exchange current density activation energy
C_{dl}	F m^{-2}	Electrical double layer capacitance
R_{film}	Ω m^2	Film resistance
α	-	Charge transfer coefficient
D_e	m^2 s^{-1}	Electrolyte diffusion coefficient
κ	S m^{-1}	Initial electrolyte conductivity
$E_{act,\kappa}$	J mol^{-1}	Ionic conductivity activation energy
t_0^{+}	-	Transference number
σ	S m^{-1}	Electronic conductivity
$E_{act,\sigma}$	J mol^{-1}	Electronic conductivity activation energy
D_s	m^2 s^{-1}	Solid diffusion coefficient
$E_{act,Ds}$	J mol^{-1}	Solid diffusion activation energy
L	m	Thickness
R_s	m	Active material particle radius
ρ_{He}	kg m^{-3}	Absolute density (helium pycnometry measurement)
ρ_{Hg}	kg m^{-3}	Bulk density (mercury intrusion porosimetry measurement)
ε_e	-	Porosity / Pore volume fraction
ε_s	-	Solid volume fraction
τ	-	Electrode tortuosity
a_s	m^2 m^{-3}	Specific surface area
W	m	Cell electrode width
H	m	Cell electrode heigth
N_{elec}	-	Number of electrodes within a cell
A_{cell}	m^2	Full-cell cross sectional area (based on positive electrode W a
A_{coin}	m^2	Coin-cell cross sectional area (12 mm diameter disc)
U_{cell}	V	Cell open-circuit voltage
Li_{loss}	-	Initial lithium inventory loss during formation cycling
Q_{excess}	-	Negative electrode excess host capacity

V_{max}	V	Cell maximum voltage
V_{min}	V	Cell minimum voltage
T	K	Cell temperature
i_{cell}	A m^{-2}	Total current density per geometric area (A_{cell} or A_{coin})

References

[1] D. Miranda, C.M. Costa, S. Lanceros-Mendez, Review: Lithium ion rechargeable batteries: state of the art and future needs of microscopic theoretical models and simulations, J. Electroanal. Chem. 739 (2015) 97–110, doi:10.1016/j.jelechem.2014.12.010.

[2] World Economic Forum, A vision for a sustainable battery value chain in 2030 unlocking the full potential to power sustainable development and climate change mitigation, 2019.

[3] A.A. Franco, Multiscale modelling and numerical simulation of rechargeable lithium ion batteries: concepts, methods and challenges, RSC Adv 3 (2013) 13027–13058, doi:10.1039/c3ra23502e.

[4] J. Newman, W. Tiedemann, Porous electrode theory with battery applications, AIChE J. 21 (1975) 25–41, doi:10.1002/aic.690210103.

[5] M. Doyle, T.F. Fuller, J. Newman, Modeling of Galvanostatic charge and discharge of the lithium/polymer/insertion cell, J. Electrochem. 140 (1993) 1526–1533, doi:10.1149/1.2221597.

[6] T.F. Fuller, M. Doyle, J. Newman, Relaxation phenomena in lithium-ion-insertion cells, J. Electrochem. Soc. 141 (1994) 982–990, doi:10.1149/1.2054868.

[7] M. Doyle, J. Newman, The use of mathematical modeling in the design of lithium/polymer battery systems, Electrochim. Acta. 40 (1995) 2191–2196, doi:10.1016/0013-4686(95)00162-8.

[8] M. Doyle, J. Newman, A.S. Gozdz, C.N. Schmutz, J.-M. Tarascon, Comparison of modeling predictions with experimental data from plastic lithium ion cells, J. Electrochem. Soc. 143 (1996) 1890–1903.

[9] I.J. Ong, J. Newman, Double-layer capacitance in a dual lithium ion insertion cell, J. Electrochem. Soc. 146 (1999) 4360–4365, doi:10.1149/1.1392643.

[10] G. Plett, Battery Management Systems: Battery Modeling, Volume I, Artech House, 2015.

[11] R. Jobman, M.S. Trimboli, G.L. Plett, Identification of lithium-ion physics-based model parameter values, J. Energy Challenges Mech. 2 (2015) 45–55.

[12] J. Vazquez-Arenas, L.E. Gimenez, M. Fowler, T. Han, S.K. Chen, A rapid estimation and sensitivity analysis of parameters describing the behavior of commercial Li-ion batteries including thermal analysis, Energy Convers. Manag. 87 (2014) 472–482, doi:10.1016/j.enconman.2014.06.076.

[13] A. Jokar, B. Rajabloo, M. Désilets, M. Lacroix, An inverse method for estimating the electrochemical parameters of lithium-ion batteries i. methodology, J. Electrochem. Soc. 163 (2016) A2876–A2886, doi:10.1149/2.0191614jes.

[14] B. Rajabloo, A. Jokar, M. Désilets, M. Lacroix, An inverse method for estimating the electrochemical parameters of lithium-ion batteries II: implementation, J. Electrochem. Soc. 164 (2017) A99–A105, doi:10.1149/2.0221702jes.

[15] L. Zhang, C. Lyu, G. Hinds, L. Wang, W. Luo, J. Zheng, K. Ma, Parameter sensitivity analysis of cylindrical LiFePO4 battery performance using multi-physics modeling, J. Electrochem. Soc. 161 (2014) A762–A776, doi:10.1149/2.048405jes.

[16] R.R. Jobman, Identification of Lithium-Ion-Cell Physics-Model Parameter Values, University of Colorado Colorado Springs, 2016.

[17] Z. Chu, R. Jobman, A. Rodríguez, G.L. Plett, M.S. Trimboli, X. Feng, M. Ouyang, A control-oriented electrochemical model for lithium-ion battery. Part II: Parameter identification based on reference electrode, J. Energy Storage. 27 (2020) 101, doi:10.1016/j.est.2019.101101.

[18] A. Falconi, Electrochemical Li-Ion Battery Modeling for Electric Vehicles, Communaute Universite Grenoble Alpes, 2018.

[19] M. Doyle, Y. Fuentes, Computer simulations of a lithium-ion polymer battery and implications for higher capacity next-generation battery designs, J. Electrochem. Soc. 150 (2003) A706–A713, doi:10.1149/1.1569478.

[20] W. Fang, O.J. Kwon, C.-Y. Wang, Electrochemical-thermal modeling of automotive Li-ion batteries and experimental validation using a three-electrode cell, Int. J. Energy Res. 34 (2010) 107–115, doi:10.1002/er.1652.

[21] M. Safari, C. Delacourt, Mathematical modeling of lithium iron phosphate electrode: galvanostatic charge/discharge and path dependence, J. Electrochem. Soc. 158 (2011) A63–A73, doi:10.1149/1.3515902.

[22] E. Prada, D. Di Domenico, Y. Creff, J. Bernard, V. Sauvant-Moynot, F. Huet, Simplified electrochemical and thermal model of LiFePO4-graphite li-ion batteries for fast charge applications, J. Electrochem. Soc. 159 (2012) A1508–A1519, doi:10.1149/2.064209jes.

[23] M. Ecker, T.K.D. Tran, P. Dechent, S. Kabitz, A. Warnecke, D.U. Sauer, Parameterization of a physico-chemical model of a lithium-ion battery: I. determination of parameters, J. Electrochem. Soc. 162 (2015) A1836–A1848, doi:10.1149/2.0551509jes.

[24] M. Ecker, S. Kabitz, I. Laresgoiti, D.U. Sauer, Parameterization of a physico-chemical model of a lithium-ion II . Model validation, J. Electrochem. Soc. 162 (2015) A1849–A1857, doi:10.1149/2.0541509jes.

[25] M. Ecker, Lithium Plating in Lithium-Ion Batteries, RWTH Aachen University, 2016.

[26] J. Schmalstieg, Physikalisch-Elektrochemische Simulation von Lithium-Ionen-Batterien. Implementierung, Parametrierung und Anwendung, RWTH Aachen University, 2017.

[27] J. Schmalstieg, C. Rahe, M. Ecker, D.U. Sauer, Full cell parameterization of a

[28] J. Schmalstieg, D.U. Sauer, Full cell parameterization of a high-power lithium-ion battery for a physico-chemical model: part ii. thermal parameters and validation, J. Electrochem. Soc. 165 (2018) A3811–A3819, doi:10.1149/2.0331816jes.

[29] T. Waldmann, A. Iturrondobeitia, M. Kasper, N. Ghanbari, F. Aguesse, E. Bekaert, L. Daniel, S. Genies, I. Jiménez Gordon, M.W. Löble, E. De Vito, M. Wohlfahrt-Mehrens, Review - post-mortem analysis of aged lithium-ion batteries: disassembly methodology and physico-chemical analysis techniques, J. Electrochem. Soc. 163 (2016) A2149–A2164, doi:10.1149/2.1211609jes.

[30] B. Pilipili Matadi, Study of the Aging Mechanisms of Li-ion Batteries Under Low Temperature Cycling and High Temperature Storage: Understanding of the Origins and Aging Modeling, Communaute Universite Grenoble Alpes, 2016.

[31] P. Arora, Z. Zhang, Battery separators, Chem. Rev. 104 (2004) 4419–4462, doi:10.1021/cr020738u.

[32] B. Pilipili Matadi, Study of the Aging Mechanisms of Li-ion Batteries Under Low Temperature Cycling and High Temperature Storage: Understanding of the Origins and Aging Modeling (2016).

[33] D.P. Abraham, S. Kawauchi, D.W. Dees, Modeling the impedance versus voltage characteristics of LiNi0.8Co0.15Al0.05O2, Electrochim. Acta 53 (2008) 2121–2129, doi:10.1016/j.electacta.2007.09.018.

[34] Y. Xie, J. Li, C. Yuan, Mathematical modeling of the electrochemical impedance spectroscopy in lithium ion battery cycling, Electrochim. Acta. 127 (2014) 266–275, doi:10.1016/j.electacta.2014.02.035.

[35] I.. Bobrikov, N.Y. Samoylova, S.V. Sumnikov, O.Y. Ivanshina, R.N. Vasin, A.I. Beskrovnyi, A.M. Balagurov, In-situ time-of-flight neutron diffraction study of the structure evolution of electrode materials in a commercial battery with LiNi0.0Co0.15Al0.05O2 cathode, J. Power Sourc. 372 (2017) 74–81.

[36] J. Akimoto, Y. Gotoh, Y. Oosawa, Synthesis and structure refinement of LiCoO2 single crystals, J. Solid State Chem. 141 (1998) 298–302, doi:10.1006/jssc.1998.7966.

[37] P. Trucano, R. Chen, Structure of graphite by neutron diffraction, Nature 258 (1975) 136–137.

[38] Y. Idemoto, Y. Takanashi, N. Kitamura, Dependence of property, crystal structure and electrode characteristics on Li content for LixNi0.8Co0.2O2 as a cathode active material for Li secondary battery, J. Power Sourc. 189 (2009) 269–278, doi:10.1016/j.jpowsour.2008.09.048.

[39] M. Mayur, M.C. Yagci, S. Carelli, P. Margulies, D. Velten, W.G. Bessler, Identification of stoichiometric and microstructural parameters of a lithium-ion cell with blend electrode, Phys. Chem. Chem. Phys. 21 (2019) 23672–23684, doi:10.1039/c9cp04262h.

[40] G. Fuchs, L. Willenberg, F. Ringbeck, D.U. Sauer, Post-mortem analysis of inhomogeneous induced pressure on commercial lithium-ion pouch cells and their effects, Sustainability 11 (2019) 6738–6751, doi:10.3390/su11236738.

[41] J.S. Diaz-Ortiz, M.I. Delgado-Rosero, N.M. Jurado-Meneses, G.M. Aparicio-Rojas, Thermal analysis and mass spectrometry in protonic conductors (PVDF/H3PO2) for implementation in fuel cells, DYNA 85 (2018) 143–149, doi:10.15446/dyna.v85n204.66968.

[42] M.J. Fernández-Berridi, N. González, A. Mugica, C. Bernicot, Pyrolysis-FTIR and TGA techniques as tools in the characterization of blends of natural rubber and SBR, Thermochim. Acta. 444 (2006) 65–70, doi:10.1016/j.tca.2006.02.027.

[43] V. Mishra, R. Kumar, Graft copolymerization of carboxymethylcellulose: an overview, Trends Carbohydr. Res. 4 (2012) 1–17.

[44] N. Dufour, Physics-Based Modeling of Graphite Electrodes inside Lithium-ion Battery: Study of Lithiation Heterogeneities and Aging Mechanisms, Communaute Universite Grenoble Alpes, 2016.

[45] R.P.D. Amelia, S. Gentile, W.F. Nirode, L. Huang, Quantitative analysis of copolymers and blends of polyvinyl acetate (PVAc) using fourier transform infrared spectroscopy (FTIR) and elemental analysis (EA), World J. Chem. Educ. 4 (2016) 25–31, doi:10.12691/wjce-4-2-1.

[46] B. Pilipili Matadi, S. Geniès, A. Delaille, T. Waldmann, M. Kasper, M. Wohlfahrt-Mehrens, F. Aguesse, E. Bekaert, I. Jiménez-Gordon, L. Daniel, X. Fleury, M. Bardet, J.F. Martin, Y. Bultel, Effects of biphenyl polymerization on lithium deposition in commercial graphite/NMC lithium-ion pouch-cells during calendar aging at high temperature, J. Electrochem. Soc. 164 (2017) A1089–A1097, doi:10.1149/2.0631706jes.

[47] R. Castaing, P. Moreau, Y. Reynier, D. Schleich, S.Jouanneau Si Larbi, D. Guyomard, N. Dupré, NMR quantitative analysis of solid electrolyte interphase on aged Li-ion battery electrodes, Electrochim. Acta. 155 (2015) 391–395, doi:10.1016/j.electacta.2014.12.049.

[48] R. Petibon, L. Rotermund, K.J. Nelson, A.S. Gozdz, J. Xia, J.R. Dahn, Study of electrolyte components in li ion cells using liquid-liquid extraction and gas chromatography coupled with mass spectrometry, J. Electrochem. Soc. 161 (2014) A1167–A1172, doi:10.1149/2.117406jes.

[49] C.R. Birkl, E. McTurk, M.R. Roberts, P.G. Bruce, D.A. Howey, A parametric open circuit voltage model for lithium ion batteries, J. Electrochem. Soc. 162 (2015) A2271–A2280, doi:10.1149/2.0331512jes.

[50] D. Aurbach, B. Markovsky, M.D. Levi, E. Levi, A. Schechter, M. Moshkovich, Y. Cohen, New insights into the interactions between electrode materials and electrolyte solutions for advanced nonaqueous batteries, J. Power Sourc. 81–82 (1999) 95–111, doi:10.1016/S0378-7753(99)00187-1.

[51] M. Ecker, Lithium Plating in Lithium-Ion Batteries. An Experimental and Simulation Approach, RWTH Aachen University, 2016.

[52] A. Nyman, An experimental and theoretical study of the mass transport in lithium-ion battery electrolytes, KTH Chem. Sci. Eng. (2011).

[53] A. Falconi, Electrochemical Li-Ion Battery Modeling for Electric Vehicles, Communaute Universite Grenoble Alpes, 2018.

[54] J. Schmalstieg, Physikalisch-Elektrochemische Simulation von Lithium-Ionen-Batterien. Implementierung, Parametrierung und Anwendung, RWTH Aachen University, 2015.

[55] H. Anne, Understanding the Kinetic Limitations of NaFePO4 as Cathode Active Material for Na-ion Battery, Basque Country University, 2019.

[56] J. Christensen, Modeling diffusion-induced stress in Li-ion cells with porous electrodes, J. Electrochem. Soc. 157 (2010) A366–A380, doi:10.1149/1.3269995.

[57] M. Ebner, D.W. Chung, R.E. García, V. Wood, Tortuosity anisotropy in lithium-ion battery electrodes, Adv. Energy Mater. 4 (2013) 1–6, doi:10.1002/aenm.201301278.

[58] A. Kwade, W. Haselrieder, R. Leithoff, A. Modlinger, F. Dietrich, K. Droeder, Current status and challenges for automotive battery production technologies, Nat. Energy. 3 (2018) 290–300, doi:10.1038/s41560-018-0130-3.

[59] L. Froboese, P. Titscher, B. Westphal, W. Haselrieder, A. Kwade, Mercury intrusion for ion- and conversion-based battery electrodes - structure and diffusion coefficient determination, Mater. Charact. 133 (2017) 102–111, doi:10.1016/j.matchar.2017.09.002.

[60] S.C. Carniglia, Construction of the tortuosity factor from porosimetry, J. Catal. 102 (1986) 401–418, doi:10.1016/0021-9517(86)90176-4.

[61] M. Ebner, D.W. Chung, R.E. García, V. Wood, Tortuosity anisotropy in lithium-ion battery electrodes, Adv. Energy Mater. 4 (2014), doi:10.1002/aenm.201301278.

[62] M. Mayur, M.C. Yagci, S. Carelli, P. Margulies, D. Velten, W.G. Bessler, Identification of stoichiometric and microstructural parameters of a lithium-ion cell with blend electrode, Phys. Chem. Chem. Phys. 21 (2019) 23672–23684, doi:10.1039/c9cp04262h.

[63] L. Xie, D. Ren, L. Wang, Z. Chen, G. Tian, K. Amine, X. He, A facile approach to high precision detection of cell-to-cell variation for li-ion batteries, Nature 10 (2020) 1–10, doi:10.1038/s41598-020-64174-2.

[64] A. Devie, G. Baure, M. Dubarry, Intrinsic variability in the degradation of a batch of commercial 18650 lithium-ion cells, Energies 11 (2018) 1–14, doi:10.3390/en11051031.

[65] F. An, L. Chen, J. Huang, J. Zhang, P. Li, Rate dependence of cell-to-cell variations of lithium-ion cells, Nature 6 (2016) 4–10, doi:10.1038/srep35051.

[66] E. Sarasketa-Zabala, A Novel Approach for Li-ion Battery Selection and Lifetime Prediction, Mondragon Goi Eskola Politeknikoa, 2014.

[67] G. Plett, Battery Management Systems, II, Artech House, 2015.